

Probing Primordial Black Hole Mergers in Clusters with Pulsar Timing Data

Sébastien Clesse^a, Virgile Dandoy^a, and Sonali Verma^a

^a*Service de Physique Théorique,
Brussels Laboratory of the Universe BLU-ULB,
Université Libre de Bruxelles, Boulevard du Triomphe,
CP225, 1050 Brussels, Belgium*

We consider the possibility that the stochastic gravitational wave (GW) background suggested by Pulsar Timing Array (PTA) datasets is sourced by Primordial Black Holes (PBHs). Specifically, we perform a Bayesian search in the International PTA Data Release 2 (IPTA DR2) for a combined GW background arising from scalar perturbations and unresolved PBH mergers, assuming a broad PBH mass distribution. In our analysis, we incorporate constraints on the curvature power spectrum from CMB μ -distortions and the overproduction of PBHs, which significantly suppress the contribution of PBH mergers to the total GW background. We find that scalar-induced GWs dominate the nHz frequency range, while PBH mergers alone cannot account for the observed signal under the standard PBH formation scenario involving Gaussian perturbations, and including only Poissonian PBH clustering. However, specific PBH models, such as those with enhanced clustering, could yield a GW background dominated by PBH mergers. Overall, we find that the IPTA DR2 strongly favors an astrophysical origin for the reported common-spectrum process over the PBH models considered in this analysis.

CONTENTS

		1. μ -Distortions	18
		2. ΔN_{eff}	19
		3. LVK-Constraint	19
I. Introduction	1		
II. PBH mass function from a Power Law primordial spectrum	3	E. Choice of Window Function	19
III. Scalar Induced Gravitational Waves	5	F. Full Posterior Distributions	19
IV. GW background from PBH binaries	6	References	21
A. PBH merger rate from early binaries	6		
B. PBH merger rate in late-Universe halos	7		
C. SGWB from unresolved PBH binaries	8		
V. Results and interpretation of PTA data	9		
A. Fixed Clustering Factor Analysis	9		
B. Free Clustering Factor Analysis	11		
VI. PBH Constraints	11		
VII. Conclusion and Discussion	13		
Acknowledgments	15		
A. Scalar Induced GWs	15		
B. Thermal average of binary cross-section	15		
C. PBH Clustering	16		
1. Poisson fluctuations from PBHs	16		
2. Cluster formation	16		
a. Characteristic PBH Halo Mass	16		
b. PBH Cluster Radius	17		
3. Dynamical heating of PBH clusters	17		
4. Clustering factor $R_{\text{cl}}(z)$	18		
D. Constraints on the Primordial Power Spectrum	18		

I. INTRODUCTION

Primordial Black Holes (PBHs) [1–4] might have formed in the early radiation-dominated universe from the collapse of large density perturbations upon horizon re-entry. Such large perturbations on small scales (or comoving wavenumber $k \gg 1 \text{ Mpc}^{-1}$) required for substantial PBH formation can be efficiently produced in many inflationary models (for examples see refs. [5–7]). Additional PBH formation mechanisms can also be considered, for example, PBH formation can occur during a first order cosmological phase transition [8–11], or from the collapse of bubbles nucleated during inflation [12] (see also Ref. [13]). The existence of PBHs would thus, be connected to new physics in the early universe.

For PBH formation from the direct collapse of primordial density perturbations, the PBH mass is roughly given by the size of the cosmological horizon at the time of the collapse. PBHs, thus, can have a wide range of masses, not limited by the Chandrasekhar limit [14], unlike stellar-origin black holes. In fact, the detection of a sub-solar mass black hole is considered to be the most robust smoking gun signature of a primordial origin. Several candidates have recently been identified [15–18] but without enough significance to firmly claim a detection.

PBHs may have contributed to black hole merger

events detected by the LIGO-Virgo-KAGRA (LVK) Collaboration (see for e.g., Refs. [19, 20] for PBH explanation of events GW190814 [21] and GW190521 [22]). Moreover, PBHs could also explain the dark matter (DM) or a fraction of it. These motivations have resulted in the growing interest for PBHs and ways to test these scenarios, primarily at gravitational wave experiments (see Ref. [23] for review).

Unresolved PBH binary mergers would also contribute to a stochastic gravitational wave background (SGWB). Furthermore, a GW background can also be sourced as a consequence of the mechanism responsible for PBH formation itself. For example, in the standard scenario for PBH formation which relies on the collapse of large primordial density perturbations, an SGWB is unavoidably induced by scalar perturbations at second order in perturbation theory [24–26].

A unique probe to study the gravitational-wave background (GWB) in the nano-Hertz (nHz) frequency range is offered by Pulsar Timing Arrays (PTA). Recent results released by the NANOGrav [27, 28], EPTA (in combination with InPTA) [29, 30], PPTA [31] and CPTA [32] collaborations along with the joint International PTA [33] provide the first convincing evidence for a stochastic GW spectrum in the nHz frequency range, with around $2-4\sigma$ significance for a Hellings-Downs correlation [34]. The origin of this GW background is still unknown, the prime explanation being a population of inspiralling supermassive black hole binaries (SMBHBs). Alternatively, the signal could have a cosmological origin. See for example Refs. [35, 36] for a comparison between possible models.

A PBH interpretation of the PTA signal has been widely investigated in literature [37–50]. These works have either considered only the scalar-induced GW background [36–42, 44–48], or else considered that the PTA GW background arises entirely from supermassive PBH binaries in the early Universe [49, 50]. We are not aware of any study of PTA data which considers all the relevant GW backgrounds associated to PBHs i.e. the scalar-induced GWs (SIGWs) as well as PBH mergers, for the case of broad PBH mass distributions.

In this work, we systematically address this problem and assess whether the GWB contribution from PBH binaries could be substantial enough to compete with that from SIGWs. In our analysis, instead of using a commonly assumed monochromatic or lognormal PBH mass function, we have computed the PBH merger rates for a PBH mass function starting from first principles. For a realistic phenomenological PBH model, the computation of a PBH mass function takes into account the primordial power spectrum of curvature perturbations, \mathcal{P}_ζ , corresponding to small scales ($k \gg k_{\text{CMB}} \sim 1 \text{ Mpc}^{-1}$). In addition, we have considered the effect of the lowering of the equation of state w , (with respect to its value in the radiation-dominated universe, $w = 1/3$) associated to an enhancement in PBH production associated to those scales [51] plus the effect of this variation on the collapse process itself.

For the SGWB from PBH mergers, we have considered two channels for PBH binary formation: *i*) early PBH binaries, which form when a PBH pair decouples from the Hubble flow in the early radiation-dominated Universe, and *ii*) late PBH binaries, which can form dynamically inside Poisson-induced PBH halos or clusters, forming right after matter-radiation equality. The merger rate from both these channels have many uncertainties as we discuss in section IV.

A crucial aspect of our analysis is the consideration of mergers rates of dynamically formed late-time PBH binaries in halos. Poisson fluctuations¹ in the PBH number density will inevitably lead to the formation of small scale PBH halos or clusters with varying cluster mass. Furthermore, these PBH halos can further expand in radius with time due to gravitational heating from PBHs [53, 54] with the smallest halos evaporating. In our work, we address these aspects and provide a detailed template for such merger rate computations for a broad PBH mass distribution. While our main conclusions exclude the possibility (in line with Refs. [49, 50]) of explaining the PTA signal with only PBH mergers, our analysis with respect to previous works is more rigorous. Our analysis template can be useful for such searches for PBH associated GW backgrounds at other GW experiments like LVK, and future LISA.

Before our analysis, Ref. [55] has previously considered the scenario of an SGWB in the nHz frequency range originating from PBH binaries with a broad mass distribution. As opposed to a monochromatic PBH distribution usually considered in literature, a broad PBH mass distribution features various peaks, most notably a strong peak at PBH mass $m \sim 1 M_\odot$ corresponding to the QCD epoch in the Standard Model (SM) at a temperature $T \sim 100 \text{ MeV}$ [51]. Peaks in the broad mass distribution correspond to the lowering of the equation of state w of the Universe due to decoupling of SM particles. The analysis of Ref. [55] showed that the GWB from PBH binaries forming in the late-time Universe inside PBH halos could be probed with PTA observations. This large GWB from PBH mergers was identified with a large number of merger events from PBH binaries with asymmetric masses (typically $m_1 \sim 2 M_\odot$ and $m_2 \sim 10^2 - 10^5 M_\odot$). PBH binaries, forming in the early Universe, much before the matter-radiation equality, on the other hand, result in a GW background that is much more peaked in the LVK frequency range corresponding to $\sim 10 \text{ Hz}$ [55]. Contrary to the conclusions in Ref. [55], we find that this enhancement from asymmetric binaries is greatly reduced due to the cut-off at large scales in the primordial power spectrum from CMB μ -distortions [56], which restricts the PBH mass range in merger rates to

¹ Note that we often call this inevitable effect of Poisson fluctuations as “clustering”, however, it is not to be confused with PBH clustering at formation which is negligible for the case in which the curvature perturbations follow Gaussian statistics [52].

$m \lesssim 1000 M_\odot$.

In this paper, for a PBH phenomenological model with a broad mass function, we perform a Bayesian analysis of the International PTA data release 2 (IPTA DR2) [57] to investigate the possibility that the observed PTA signal can arise from a combination of SIGWs and PBH mergers. While our results show that the scalar induced GWs dominate the GWB from PBH mergers for a broad PBH mass function derived using Gaussian curvature perturbations, we also investigate the enhancement in PBH merger rates required to explain the PTA signal with only PBH mergers. For example, a much more dense PBH cluster or enhanced PBH clustering could possibly lead to much enhanced merger rates with respect to our computations. To account for this enhancement and various other uncertainties in the merger rates (discussed in Section IV A), we take a phenomenological approach and treat the parameter for clustering as a free parameter and additionally perform a Bayesian search with this nuisance parameter. An enhancement of merger rates for early PBH binaries for highly clustered PBH distributions has been previously studied in Refs. [58–60].

As a result of these Bayesian analyses, we derive posterior probability distributions for the parameters of the primordial power spectrum, namely, the amplitude and the spectral tilt. We finally compare the predictive posterior PBH mass function derived from the Bayesian search with IPTA data in relation to other constraints on PBHs.

This paper is structured as follows: in Sec. II we review the mechanism of PBH formation and the mass function obtained in the case of a broad primordial power spectrum of curvature perturbations. In Sec. III and Sec. IV we review the GWB induced by scalar perturbations at second order and from PBH binaries, respectively. The results of the Bayesian analysis are presented in Sec. V. In Sec. VI, we discuss results in relation to other PBH constraints. We finally conclude in Sec. VII and envisage some perspectives. We further give details of our calculations in appendices: on SIGWs (Appendix A), binary formation cross-section (Appendix B), PBH halo formation (Appendix C), and related computation on the clustering factor (Appendix C 4), primordial power spectrum constraints (Appendix D), and choice of window function for PBH abundance (Appendix E). Finally, our full posterior distributions are given in Appendix F.

II. PBH MASS FUNCTION FROM A POWER LAW PRIMORDIAL SPECTRUM

In this section, we summarize the derivation of the PBH mass distribution obtained from the collapse of curvature perturbations in the Press-Schechter formalism, broadly following Ref. [61].

The standard PBH formation scenario relies on the assumption of large primordial curvature fluctuations ζ at small scales, parameterized by the curvature power spectrum $\mathcal{P}_\zeta(k)$. At horizon crossing, a PBH is formed from

the collapse of an overdensity of amplitude δ (generated by the perturbation ζ) if it exceeds a critical threshold denoted by δ_c .

The PBH mass is then approximately close to the horizon mass at re-entry

$$M_H(k) = 4\pi M_p^2/H \quad (1)$$

$$\simeq 20 M_\odot \left(\frac{k}{10^6 \text{ Mpc}^{-1}} \right) \left(\frac{g_{*,s}^4(T_{\text{cr}})g_*^{-3}(T_{\text{cr}})}{17.25} \right)^{-1/6} \quad (2)$$

with T_{cr} being the temperature at horizon crossing given by $k = aH(T_{\text{cr}})$, and $g_*(T)$ and $g_{*,s}(T)$ are the temperature dependent effective number of relativistic degrees of freedom, contributing to the energy density and entropy density respectively.

Below we review the calculation for the PBH mass function obtained from a power law primordial spectrum of the form

$$\mathcal{P}_\zeta(k) = A_\zeta \left(\frac{k}{k_*} \right)^{(n_s-1)} \Theta(k - k_{\text{min}})\Theta(k_{\text{max}} - k), \quad (3)$$

where A_ζ is the amplitude at small scales, $k_* = 10^6 \text{ Mpc}^{-1}$ is an arbitrary pivot scale here, fixed to correspond to $M_{H_*} \approx 1 M_\odot$, n_s is the spectral tilt and k_{min} , k_{max} are the cut-off scales at large and small scales respectively, introduced so as to not violate the current constraints from the CMB μ -distortions [56]. The higher cut-off k_{max} is only relevant for $n_s \gtrsim 1$ and is introduced in order to not overproduce small-mass PBHs. For broad mass distributions obtained for values of $n_s \sim 1$, the behaviour of the equation of state of the Universe $w(T)$ with temperature, specially during the QCD epoch, can play an important role [51, 62]. A non-negligible change in the effective number of degrees of freedom, $g_*(T), g_{*,s}(T)$, with temperature, leads to a transient reduction in the value of $w(T) \equiv p/\rho = 4g_{*,s}(T)/3g_*(T) - 1$, below its constant value of $1/3$ during the radiation dominated Universe. This translates into a simultaneous variation of the critical threshold δ_c [51, 62]. Hence, the PBH mass distribution is imprinted by the periods where w and consequently the critical threshold decrease. This is, for instance, the case at the QCD crossover, when quarks confine into hadrons, resulting in an enhanced density of solar-mass PBHs. For the same reason, the W^\pm and Z bosons decoupling would enhance the PBH production around $10^{-5} M_\odot$ and the e^+e^- decoupling around $10^6 M_\odot$ [62].

Under the Press-Schechter formalism of spherical collapse [63] and assuming Gaussian perturbations, the fraction of the radiation energy density that collapses into PBHs of mass m when the scale k^{-1} re-enters the horizon is given by [64, 65]

$$\beta_k(m) = \int_{\delta_c}^{\infty} d\delta \frac{m(\delta)}{M_H(k)} P_k(\delta) \delta_D \left[\ln \frac{m}{m(\delta)} \right]. \quad (4)$$

Here, δ^2 is the smooth density contrast at linear order and δ_D is the Dirac delta function. The function $m(\delta)$ [66–69] represents the actual mass of the PBHs formed from the collapse of the overdensity δ , $m(\delta) = \kappa M_H(k) (\delta - \frac{1}{4\Phi}\delta^2 - \delta_c)^\gamma$ where $\gamma \simeq 0.36$ is the universal critical exponent during the radiation dominated Universe [69], and κ is a parameter depending on the particular shape of the density contrast. We set $\kappa \simeq 4$ [69], the typical value obtained for a nearly-scale invariant spectrum of Gaussian primordial fluctuations. The function $P_k(\delta)$ in Eq. (4) is the Gaussian probability density function of the linear density contrast δ , at scale k

$$P_k(\delta) = \frac{1}{\sqrt{2\pi}\sigma_k} e^{-\delta^2/(2\sigma_k^2)}, \quad (5)$$

with the variance σ_k^2 at scale k given by [65, 69]

$$\sigma_k^2 = \frac{4}{9}\Phi^2 \int_0^\infty \frac{dk'}{k'} \left(\frac{k'}{k}\right)^4 T^2(k', k) W^2(k', k) \mathcal{P}_\zeta(k'), \quad (6)$$

where $T(k', k)$ is the linear transfer function and $W(k', k)$ is the window function used to smooth the perturbations (see Appendix E for full equations), and Φ [70] is a function depending on w of the Universe, in the radiation dominated Universe, $\Phi = 2/3$. It is important to stress that the choice of the window function has been shown to have a strong impact on the PBH abundance [48] (see also the discussion in Appendix E). Here we choose a top-hat window function.

Finally, the PBH mass function is given by [51, 65]

$$\begin{aligned} f_{\text{PBH}}(m) &\equiv \frac{1}{\rho_{\text{DM}}} \frac{d\rho_{\text{PBH}}}{d \ln(m)} \\ &= \frac{2}{\Omega_{\text{DM}}} \int d \ln k \left(\frac{M_{\text{eq}}}{M_H(k)}\right)^{1/2} \beta_k(m) \\ &= \frac{4}{\gamma \kappa^{1/\gamma} \Omega_{\text{DM}}} \int d \ln k \left(\frac{M_{\text{eq}}}{M_H(k)}\right)^{1/2} \\ &\times \left(\frac{m}{M_H(k)}\right)^{1+1/\gamma} \frac{P_k(\delta(m))}{1 - \frac{3}{4}\delta(m)}, \end{aligned} \quad (7)$$

where $\Omega_{\text{DM}} = 0.265$ is the dark matter relic abundance today, $M_{\text{eq}} = 2.7 \times 10^{17} M_\odot$ is the horizon mass at the time of matter-radiation equality and

$$\delta(m) = 2\Phi \left(1 - \sqrt{1 - \frac{1}{\Phi}(\delta_c + q^{1/\gamma})}\right), \quad (8)$$

with $q = m/\kappa M_H(k)$. In the rest of this work, we will additionally use the normalized PBH mass function, $\phi(m) \equiv f_{\text{PBH}}(m)/f_{\text{PBH}}$, given by

$$\phi(m) = \frac{1}{\rho_{\text{DM}} f_{\text{PBH}}} \frac{d\rho_{\text{PBH}}}{d \ln m}, \quad (9)$$

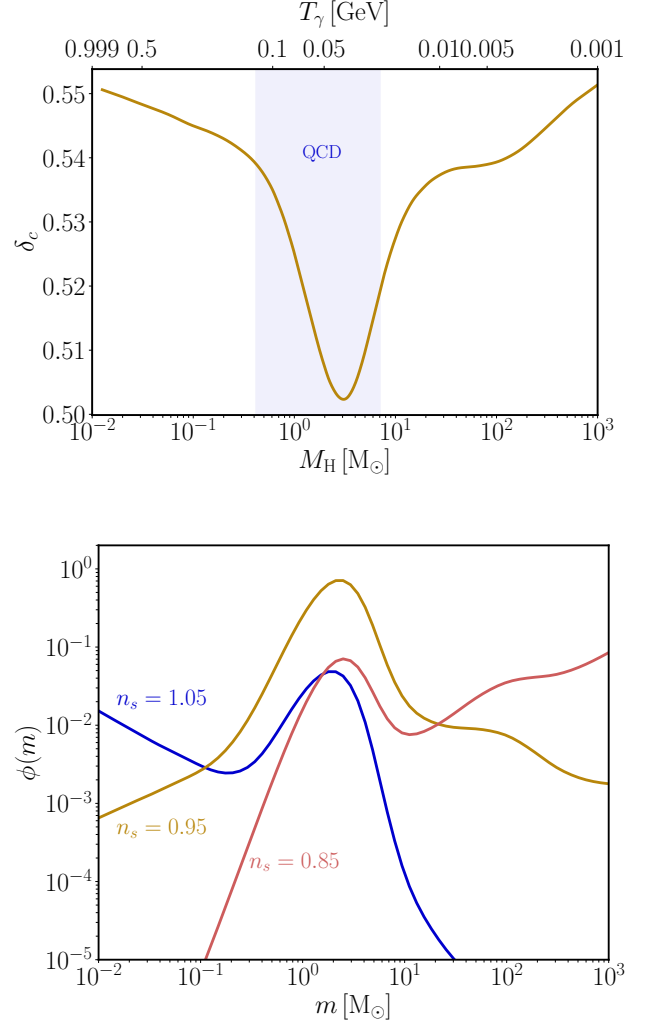


FIG. 1. **Top panel:** Evolution of the critical threshold (δ_c) for PBH formation as a function of the horizon mass (M_H) and the temperature of the Universe (T_γ). The dip around $M_H \approx 1 M_\odot$ corresponds to the QCD phase transition. Figure adapted from Ref. [70]. **Bottom panel:** PBH mass function for $n_s = 1.05$ (blue), $n_s = 0.95$ (yellow) and $n_s = 0.85$ (red). In the three cases, the amplitude of the primordial spectrum (A_ζ) has been fixed to obtain $f_{\text{PBH}} = 1$ with $k_{\text{min}} = 10^{4.5} \text{Mpc}^{-1}$, and $k_{\text{max}} = 10^9 \text{Mpc}^{-1}$.

with f_{PBH} being the fraction of DM constituted by PBHs. The function $\phi(m)$ is normalized such that $\int \phi(m) d \ln m = 1$.

Using this formalism, we calculate the PBH mass function for the primordial power spectrum defined in Eq. (3). According to Refs. [70–74], the critical threshold δ_c must be carefully calculated as a function of the primordial power spectrum shape. In the case of the spectrum in Eq. (3), it has been shown that $\delta_c \approx 0.55$ [70]. Moreover, we also consider the effect of the change of w of the Universe on δ_c . In Fig. 1, we

² Note that δ here is δ_l in the notation of Ref. [61].

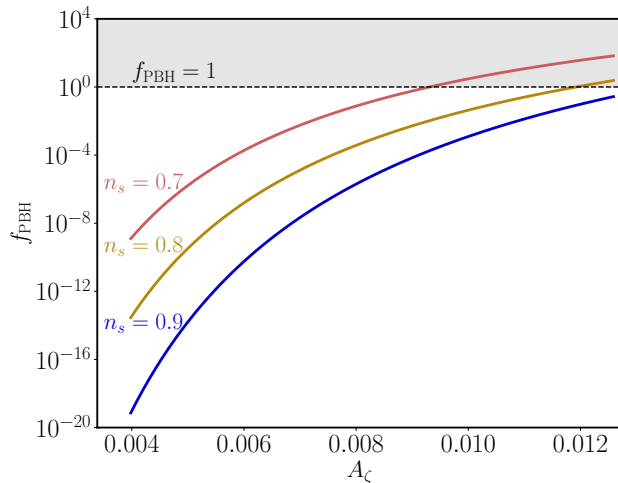


FIG. 2. Total PBH abundance as a function of the amplitude A_ζ and the power spectral index n_s of small-scale primordial fluctuations. In this example, we set $k_{\min} = 10^{4.5} \text{Mpc}^{-1}$ and $k_{\max} = 10^9 \text{Mpc}^{-1}$.

show the evolution of the critical threshold as a function of the horizon mass M_H [70]. As already discussed, δ_c reaches its lowest value around the QCD epoch.

In the bottom panel of Fig. 1 we show the corresponding mass functions for three choices of the spectral index: $n_s = 1.05$, $n_s = 0.95$ and $n_s = 0.85$ (for each, $k_{\min} = 10^{4.5} \text{Mpc}^{-1}$ and $k_{\max} = 10^9 \text{Mpc}^{-1}$). For $n_s \approx 0.95$, the mass function peaks at the solar mass level corresponding to the lowering of δ_c during the QCD epoch. For $n_s < 0.85$, the mass function peaks at large PBH mass, roughly corresponding to the horizon mass at k_{\min} . While for $n_s > 1.05$, the mass function peaks at low PBH mass, roughly corresponding to the horizon mass at k_{\max} .

As already pointed out in numerous papers (see for instance Refs. [48, 75]), the final PBH abundance f_{PBH} is exponentially sensitive to the primordial power amplitude A_ζ (through the variance σ_k^2 defined in Eq. (6)).

This sensitivity of f_{PBH} on the primordial spectrum parameters is illustrated in Fig. 2.

III. SCALAR INDUCED GRAVITATIONAL WAVES

A stochastic spectrum of second-order GWs is induced by scalar perturbations (see review in Ref. [76]). For Gaussian perturbations, this induced GW spectrum can be sizeable for enhanced primordial curvature perturbations at small scales, typically around $\mathcal{P}_\zeta \simeq 10^{-2}$ [77–80]. Such large curvature perturbations are typically required for PBH formation (see Sec. II). There are two

implications for PBHs. First, it is possible to exclude a scalar-induced origin of a GW background if the corresponding PBH abundance exceeds that of dark matter, i.e., $f_{\text{PBH}} > 1$ [36, 48]. Second, it is possible to completely rule out PBH formation in certain mass ranges due to the collapse of large perturbations if no GW background is observed in the corresponding GW frequency range. For the PTA signal, it has been shown that only a small portion of the primordial power spectrum parameter space typically survives after imposing $f_{\text{PBH}} < 1$ [35, 36, 41, 48, 81] unless one includes the impact of non-Gaussianity (NG) in the perturbations in computing the PBH abundance [82–85].

In the following, we summarize the calculation of SIGWs following Refs. [24–26]. The observable induced GW spectrum today is defined as $\Omega_{\text{gw},0} \equiv (1/\rho_c) d\rho_{\text{gw}}^0/d\ln f$, where f is the frequency of the GWs, ρ_{gw}^0 is the energy density in GWs today, and ρ_c is the critical energy density today. This can be expressed in terms of the induced GW spectrum in the radiation era through [24, 86]

$$\Omega_{\text{gw},0}(f) h^2 = \Omega_r^0 h^2 \left(\frac{g_*(T_{\text{RD}})}{g_*^0} \right) \times \left(\frac{g_{*,s}^0}{g_{*,s}(T_{\text{RD}})} \right)^{4/3} \Omega_{\text{gw, RD}}(f), \quad (10)$$

where $\Omega_r^0 h^2 = 4.1 \times 10^{-5}$, is the radiation density fraction today³, while $g_*^0 = 3.36$ and $g_{*,s}^0 = 3.91$. The last factor $\Omega_{\text{gw, RD}}(f)$ is the time-independent⁴ GW spectrum during the radiation dominated era (valid up to the matter-radiation equality). This can be written as a function of the curvature perturbation power spectrum [26]:

$$\Omega_{\text{gw, RD}}(k) = \frac{1}{12} \int_0^\infty dt \int_{-1}^1 ds \left[\frac{t(2+t)(s^2-1)}{(1-s+t)(1+s+t)} \right]^2 \times \bar{I}^2(u, v) \mathcal{P}_\zeta(uk) \mathcal{P}_\zeta(vk), \quad (11)$$

with the variables u and v defined in terms of the integration variables s, t as $u = (s+t+1)/2$ and $v = (t-s+1)/2$. The function $\bar{I}^2(u, v)$ appearing inside the integral is defined in Appendix A (see also Ref. [26]). Finally, we use the following expression to relate the comoving wavenumber k of the curvature mode to the frequency f of the GW spectrum:

$$f = \frac{k}{2\pi a_0} \simeq 1.6 \text{ nHz} \left(\frac{k}{10^6 \text{ Mpc}^{-1}} \right) \quad (12)$$

where $a_0 = 1$ is the scale factor today.

³ including photons as well as neutrinos

⁴ The time-independence of the GW spectrum results from averaging the oscillatory behaviour, deep inside the horizon [24], as detailed in Appendix A.

Eq. (11) shows the dependence $\Omega_{\text{gw}} \propto \mathcal{P}_\zeta^2 \propto \zeta^4$. Note that Eq. (11) assumes Gaussian perturbations ζ . We do not consider the impact of non-gaussianities, see Refs. [45, 82–85] for the inclusion of non-Gaussianities in the SIGW calculation.

Considering the power spectrum in Eq. 3, one can derive an approximate analytical expression for the induced GW spectrum today [26], given by

$$\Omega_{\text{gw},0}^{\text{SIGW}}(f) h^2 = 7.5 \times 10^{-5} g_*(T) (g_{*,s}(T))^{-4/3} Q(n_s) \times A_\zeta^2 \left(\frac{f}{f_*} \right)^{2(n_s-1)} \Theta(f - f_{\min}) \Theta(f_{\max} - f), \quad (13)$$

where $Q(n_s)$ can be computed by integrating Eq. (11) and is an $\mathcal{O}(1)$ factor [26]. For example, for $n_s = 0.9655$, one gets $Q(n_s) = 0.814$. Here, f_{\min} (f_{\max}) correspond to the k_{\min} (k_{\max}) cut-offs in the frequency space.

In the case of the spectrum defined in Eq. (3) because of the large (small)-scale cutoff k_{\min} (k_{\max}), one has to compute the SIGW spectrum numerically directly using Eq. (11). For our analysis, we used the approximate solution above for reducing the computational time.

IV. GW BACKGROUND FROM PBH BINARIES

In this section, we determine the GW spectrum from PBH binary mergers. Two main channels are commonly considered. The first one comes from early Universe PBH binaries that decoupled from the Hubble flow before matter-radiation equality [87, 88] (see also Refs. [89, 90] for detailed computations). The second channel instead relies on PBH binaries that can dynamically form in clusters via capture. The formation of such small-scale PBH clusters is inevitable due to the Poisson fluctuations in the spatial distribution of PBHs at formation [19, 54, 91, 92] (details on PBH clustering can be found in Appendix C). The formation of these small-scale PBH clusters can be described using the Press-Schechter formalism [63] (see Appendix C). N-body simulations of Ref. [93] (and more recently done in Ref. [94]) further confirm this ⁵.

In Ref. [19], it was shown that for broad mass spectra (which can be obtained from the PBH mass function defined in Eq. 7 of Sec. II for values of $n_s \simeq 1$), the GW background from late-time PBH binaries in dense clusters would be enhanced compared to the case of a monochromatic or lognormal mass function. This enhanced GW amplitude was identified in Ref. [55] as originating from the numerous binaries with asymmetric masses. Furthermore, it has been shown in Ref. [55] that for n_s close to

0.95, the GW background from clustered PBHs could reach the NANOGrav sensitivity and largely dominate over the early universe binaries which instead, dominate the GW background in the LVK frequency range corresponding to 10 Hz – 10 kHz. We note here that the conclusions of Ref. [55] were derived for a small-scale primordial spectrum without any cut-off at small wavenumber k_{\min} . Constraints from μ -distortions (see discussion in appendix D 1) from COBE/FIRAS [96, 97] which require $k_{\min} \gtrsim 10^5 \text{ Mpc}^{-1}$, will limit the formation of any PBHs above $m \gtrsim 1000 M_\odot$. In this scenario, we find that the GWB expected from late binaries will be much smaller than the one calculated in Ref. [55].

In the following subsections, we review the calculation of the GW background from PBH binaries and then discuss the merger rates for early PBH binaries and for late PBH binaries formed in small-scale clusters.

A. PBH merger rate from early binaries

As we indicated earlier, an important binary formation channel comes from PBH pairs that decoupled from the Hubble flow and formed binaries before the matter-radiation equality. The merger rate of such PBH binaries formed in the early Universe is [89]

$$\frac{d\mathcal{V}(z)_{\text{early}}}{d \ln m_1 d \ln m_2} = \frac{1.6 \times 10^6}{\text{Gpc}^3 \text{ yr}} f_{\text{PBH}}^{53/37} \left(\frac{t}{t_0} \right)^{-\frac{34}{37}} \left(\frac{M}{M_\odot} \right)^{-\frac{32}{37}} \times \eta^{-\frac{34}{37}} S(\phi, f_{\text{PBH}}, M) \phi(m_1) \phi(m_2) \quad (14)$$

where $M = m_1 + m_2$, $\eta = m_1 m_2 / M^2$, and t_0 is the age of the universe. The suppression factor $S(\phi, f_{\text{PBH}}, M) < 1$ accounts for effects in the early and late-time Universe, $S \equiv S_{\text{early}} \times S_{\text{late}}$. The suppression factor from the early Universe originates due to the interaction of PBH binaries with a third PBH as well as surrounding matter perturbations, that can disrupt the binary. This is given by (see for e.g. Ref. [89, 98])

$$S_{\text{early}} \approx 1.42 \left(\frac{\langle m^2 \rangle / \langle m \rangle^2}{\bar{N} + C} + \frac{\sigma_M^2}{f_{\text{PBH}}^2} \right)^{-21/74} \exp(-\bar{N}) \quad (15)$$

where $\sigma_M \simeq 0.004$, C is a fitting function that we take from Appendix A of Ref. [98] while \bar{N} is the expected number of PBHs that fall into the PBH binary ⁶

$$\bar{N} \approx \frac{M}{\langle m \rangle} \frac{f_{\text{PBH}}}{f_{\text{PBH}} + \sigma_M}. \quad (17)$$

⁶ Note that the averaged mass-dependent quantities above are defined in our notation as:

$$\langle X \rangle = \frac{\int X m^{-1} \phi(m) d \ln m}{\int m^{-1} \phi(m) d \ln m} \quad (16)$$

⁵ These PBH clusters could even correspond to ultra-faint dwarf galaxies [95].

PBH mass distributions with a small $\langle m \rangle$ will result in $\bar{N} \gg 1$, giving an exponential suppression in the merger rate from early binaries.

The suppression in the early merger rate in the late Universe denoted by S_{late} occurs due to the absorption of early PBH binaries by small-scale PBH clusters (see for example Ref. [90]). The suppression factor at any redshift z is accounted for by the probability of finding unperturbed PBHs outside of unstable PBH clusters. We use the following numerical fit for this suppression factor given in Ref. [98]

$$S_{\text{late}}(z=0) \approx \min[1, 9.6 \cdot 10^{-3} x^{-0.65} \exp(0.03 \ln^2 x)] \quad (18)$$

where $x = (t(z)/t_0)^{0.44} f_{\text{PBH}}$. It is important to note that the late-time suppression factor above has been computed for a monochromatic mass distribution [90]. The extension for wider mass PBH functions is non-trivial and still an open issue. We will extrapolate the result for the narrow mass distribution of Eq. (18) also for broad mass spectra. Note that for small $f_{\text{PBH}} \simeq 0.004$ [90], $S_{\text{late}}(z=0) \simeq 1$ for the monochromatic PBH mass distribution case, implying no suppression in the early merger rate from PBH cluster effect.

B. PBH merger rate in late-Universe halos

After the epoch of recombination in the late Universe, PBH binary formation can also take place dynamically via two-body capture. A crucial ingredient for this channel is the formation of PBH clusters due to the enhanced matter power spectrum at small scales, inevitably induced by the Poisson fluctuations in the PBH number density (see Refs. [92, 93, 99]). This small-scale structure formation can be described using the Press-Schechter formalism (more details on PBH cluster formation can be found in Appendix C). After the matter-radiation equality, these PBH clusters can form and virialize. In this section, we give details of the merger rates from PBH binaries that can form dynamically in such dense PBH clusters.

We first proceed with the calculation of the merger rate in a single PBH halo, denoted by \mathcal{R}_h . Let us consider two PBHs with masses m_1 and m_2 moving with a relative velocity v in a PBH halo of mass M_h . If the energy loss due to gravitational waves exceeds the orbital kinetic energy, the objects form a binary system. The cross-section for this binary formation process is given by [100, 101]

$$\sigma_{\text{bin}} = 2\pi \left(\frac{85\pi}{6\sqrt{2}} \right)^{2/7} \frac{G^2(m_1 + m_2)^{10/7} (m_1 m_2)^{2/7}}{c^{10/7} v^{18/7}}. \quad (19)$$

The differential merger rate per unit logarithmic mass is

then given by [102]:

$$\frac{d\mathcal{R}_h}{d \ln m_1 d \ln m_2} = \frac{4\pi}{m_1 m_2} \int_0^{r_h} dr r^2 \frac{1}{2} \left(\frac{d\rho_{\text{PBH}}(r)}{d \ln m_1} \right) \times \left(\frac{d\rho_{\text{PBH}}(r)}{d \ln m_2} \right) \langle \sigma_{\text{bin}} v \rangle. \quad (20)$$

Here the quantity $\langle \sigma_{\text{bin}} v \rangle$ denotes the thermal average of the binary formation cross-section defined in Eq. (19), whose detailed calculation can be found in Appendix B. The local PBH density distribution in the halo is captured by $d\rho_{\text{PBH}}(r)/d \log m = \rho_{\text{NFW}}(r) f_{\text{PBH}} \phi(m)$, where $\phi(m)$ is the PBH mass distribution defined in Eq. (9) and $\rho_{\text{NFW}}(r)$ is the density profile of the cluster. We have assumed a Navarro-Frenk-White (NFW) profile, $\rho_{\text{NFW}}(r) = \rho_s [(r/r_s)(1 + r/r_s)^2]^{-1}$ [103], with a characteristic radius r_s and characteristic density ρ_s . r_h is the Virial radius of the cluster, defined as the radius where the halo density is equal to 200 times the critical cosmological density. They are related by a concentration parameter C , defined as $C \equiv r_h/r_s$. The density profile of halos is fully determined once C has been expressed as a function of the halo mass M_h . Following Ref. [102], we use the concentration-mass relations from Refs. [104, 105]. The total mass of the halo within r_h is given by $M_h = 4\pi \rho_s r_s^3 g(C)$ where $g(C) = \ln(1 + C) - C/(1 + C)$.

Finally, the total cosmological merger rate of PBHs can be computed by convoluting the merger rate in a single halo \mathcal{R}_h with the halo mass function dn/dM_h , [102]

$$\frac{d\mathcal{V}(z)}{d \ln m_1 d \ln m_2} = \int_{M_{\text{min}}(z)}^{\infty} dM_c \frac{d\mathcal{R}}{d \ln m_1 d \ln m_2} \frac{dn(z)}{dM_h}, \quad (21)$$

where the halo mass function above includes haloes from Poisson fluctuations arising from the discrete nature of PBHs (see similar calculations in Refs. [106, 107]). We use the PBH halo mass function derived using the Press-Schechter formalism in Ref. [93]

$$\frac{dn(z)}{dM_h} = \frac{\bar{\rho}_{\text{PBH}}}{\sqrt{\pi}} \left(\frac{M_h}{M_*(z)} \right)^{1/2} \frac{e^{-M_h/M_*}}{M_h^2} \quad (22)$$

with $\bar{\rho}_{\text{PBH}}$ being the background PBH density today given by $\bar{\rho}_{\text{PBH}} = f_{\text{PBH}} \rho_{\text{DM}}$ and M_* being the characteristic halo mass formed at redshift z [93] (see also Eq. (C6) in appendix C)

$$M_*(z) \simeq \left(\frac{3656}{1+z} \right)^2 \langle f_{\text{PBH}}^2 m \rangle. \quad (23)$$

Compared to [91] that applied this to monochromatic or peaked mass distributions, we have averaged $f_{\text{PBH}}^2 m$ for the considered broad mass functions, replacing $f_{\text{PBH}}^2 m$ with $\langle f_{\text{PBH}}^2 m \rangle$ (see Eq. (C7) for the definition of the averaged quantity in this case). Due to the exponential cutoff in dn/dM_h at large halo masses, the upper limit of

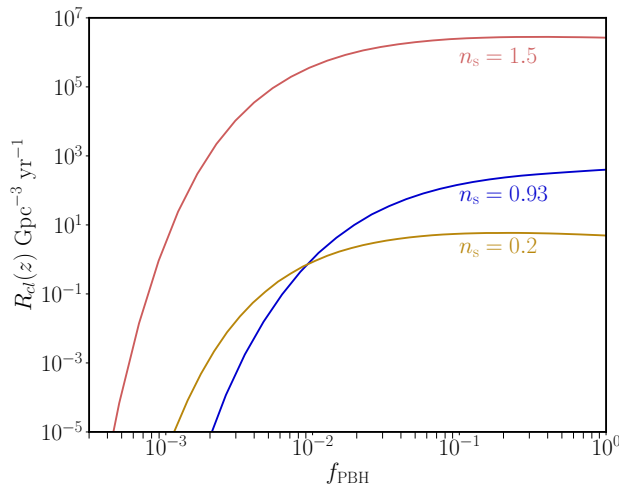


FIG. 3. The clustering parameter or R_{cl} appearing in the merger rate for late binaries in Eq. (24) (see Eq. (C15) in appendix for exact expression) as a function of f_{PBH} , evaluated at redshift $z = 0$ (today), for three different values of spectral index: $n_s = 1.5$ (red), $n_s = 0.93$ (blue), $n_s = 0.2$ (yellow).

the integral in Eq. (21) does not impact the final merger rate. Indeed, the biggest contribution to the merger rate will come from the lightest PBH halos.

The lower limit of the integral in Eq. (21), thus, must be carefully considered: once formed, PBH halos can undergo dynamical heating and therefore, expand. Eventually, the small halos are completely diluted in larger halos [54] and do not contribute to the merger rate in Eq. (21). We parameterize this effect with a lower halo mass limit $M_{\text{min}}(z)$ that encodes the lowest cluster mass that has not been diluted. The calculation of $M_{\text{min}}(z)$ is detailed in Appendix C 4.

Using Eqs. (19),(20), (9), we can now write the differential total merger rate per unit logarithmic mass, as a function of redshift

$$\frac{d\mathcal{V}(z)_{\text{late}}}{d \ln m_1 d \ln m_2} = f_{\text{PBH}}^2 R_{\text{cl}}(z) \phi(m_1) \phi(m_2) \times \frac{(m_1 + m_2)^{10/7}}{(m_1 m_2)^{5/7}}, \quad (24)$$

where we have introduced $R_{\text{cl}}(z)$, a dimensionful factor (in units of $\text{Gpc}^{-3} \text{yr}^{-1}$) containing clustering information, following [54]. It includes the PBH halo mass function, the dependence on the halo mass and radius, as well as the PBH cluster evolution with redshift. Details of the calculation of this factor can be found in Appendix C 4 that extend the previous estimations of [54]. We illustrate the dependence of R_{cl} on f_{PBH} for different values of n_s for $z = 0$ (today) in Fig. 3.

C. SGWB from unresolved PBH binaries

The SGWB from PBH mergers follows the standard relationship to the comoving number density of compact binary sources (for e.g. astrophysical black holes, neutron stars). We summarise this derivation here following Ref. [108] (see also e.g. Refs. [55, 70, 109, 110] for a similar derivation applied to the PBH scenario).

The spectrum of GWB expected from PBH binaries (PBHBs) today can be written as

$$\Omega_{\text{gw},0}^{\text{PBHB}}(f) = \frac{1}{\rho_c} \frac{d\rho_{\text{gw}}^0}{d \log f} = \frac{1}{\rho_c} \int_0^\infty N(z) \frac{1}{1+z} \left(f_r \frac{dE_{\text{gw}}}{df_r} \right) dz, \quad (25)$$

where $N(z)$ is the comoving number density of PBH merger events between z and $z + dz$ and $f_r (dE_{\text{gw}}/df_r)$ is the energy emitted as gravitational radiation per event between the frequency f_r and $f_r + df_r$, with $f_r = f(1+z)$, the frequency measured in the source frame and f the observed GW frequency today⁷.

We can relate $N(z)$ to the total merger rate per comoving unit volume $\mathcal{V}(z)$ through

$$N(z) = \frac{\mathcal{V}(z)}{[H(z)(1+z)]} \quad (26)$$

where $H(z) = H_0 (\Omega_m(1+z)^3 + \Omega_r(1+z)^4 + \Omega_\Lambda)^{1/2}$, with $\Omega_m = 0.315$ and $\Omega_\Lambda = 0.685$.

For the case of circular PBH binaries of masses m_1 and m_2 , in the Newtonian limit, the form of the differential GW spectrum emitted in Eq. (25) can be well-approximated by

$$\frac{dE_{\text{gw}}}{df_r} = \frac{\pi^{2/3}}{3G} \frac{(G \mathcal{M}_c)^{5/3}}{f_r^{1/3}}, \quad (27)$$

where \mathcal{M}_c is the chirp mass defined in terms of component PBH masses as $\mathcal{M}_c^{5/3} = m_1 m_2 (m_1 + m_2)^{-1/3}$. Eq. 27 is valid for $f_r < 2f_{\text{ISCO}}$ where

$$f_{\text{ISCO}} = 2.3 \text{ kHz} \left(\frac{M_\odot}{m_1 + m_2} \right) \quad (28)$$

is the frequency corresponding to the Innermost Stable Circular Orbit (ISCO). In principle, there is a lower limit on frequency coming from the initial separation of PBH binaries, but for the typical velocity dispersions in the PBH clusters we consider, this lower limit is below the nHz range [109].

⁷ Note that the differential energy dE_{gw}/df_r emitted per event is expressed in the source rest frame as well. This explains the additional factor of $(1/1+z)$ in Eq. (25), which accounts for the GW redshifting. This follows from the scaling of GW energy density as $\rho_{\text{gw}} \propto a^{-4}$.

Note that the GW spectrum given above captures the inspiral phase of any BH binary (including PBH binaries), while for the merger and ringdown phases, a completely different dependence of the spectrum on f_r is expected (see for example expressions in Ref. [111]). For PTA frequencies of \mathcal{O} (nHz), the leading contribution to the GW spectrum comes from inspiralling BHs.

We can finally express the GW spectrum from PBH binaries by plugging Eq. (24) and Eq. (14) in Eq. (25), giving

$$\Omega_{\text{gw},0}^{\text{PBHB}}(f) = f^{2/3} \frac{(\pi G)^{2/3}}{\rho_c} \int dz d \ln m_1 d \ln m_2 \quad (29)$$

$$\times \frac{1}{H(z)(1+z)^{4/3}} \frac{d\mathcal{V}(z)}{d \ln m_1 d \ln m_2} \mathcal{M}_c^{5/3}$$

with $\mathcal{V} = \mathcal{V}_{\text{early}} + \mathcal{V}_{\text{late}}$. At frequencies lower than $2f_{\text{ISCO}}$, the GW spectrum has the characteristic frequency dependence, $\Omega_{\text{gw}}(f) \sim f^{2/3}$, as expected for inspiralling binaries under the approximation of circular orbits [108].

V. RESULTS AND INTERPRETATION OF PTA DATA

In this section, we describe our analysis of the PTA dataset for a GW background sourced by a combination of scalar perturbations and PBH binaries. For fixed values of the primordial parameters ($A_\zeta, n_s, k_{\text{min}}, k_{\text{max}}$) introduced in Eq. (3), the GWB is given by summing Eq. (13) and Eq. (29), i.e.,

$$h^2 \Omega_{\text{gw}}(f) = h^2 \Omega_{\text{gw}}^{\text{SIGGW}}(f) + h^2 \Omega_{\text{gw}}^{\text{PBHB}}(f). \quad (30)$$

In a general PBH model, our search emphasizes the contribution to the GWB from SIGWs in addition to the GWB from PBH binaries. However, there can be alternative models with a suppressed SIGW background or PBH formation scenarios which do not lead to a GWB. In such cases, the total GWB would originate only from PBH binaries. We conduct a separate analysis to cover this scenario.

We perform Bayesian analyses by obtaining Monte Carlo Markov Chains (MCMC) using the publicly available code `PTArcade` [112, 113] in which we implemented the GW signal $h^2 \Omega_{\text{gw}}(f)$ in Eq. (30) from PBH mergers and scalar induced GW. In our search, we used the latest IPTA dataset (IPTA DR2) [57] which contains timing data from 65 pulsars including a combination of the following individual PTA data releases: the EPTA data release 1.0 [114], the NANOGrav 9-year data set [115], and the PPTA first data release [116, 117]. We furthermore include the pulsar white and red noise contributions according to the prescription of IPTA DR2 [33]. Following the prescription in Ref. [33], we limit the search of GW background to the first 13 frequency bins.

Our analysis is divided into two parts. For the analysis in Section V A, we compute the clustering factor R_{cl}

appearing in the late-time PBH merger rate in Eq. (24) as a function of redshift z from the primordial power spectrum parameters, following Appendix C 4, such that at any z , $R_{\text{cl}} \equiv R_{\text{cl}}(A_\zeta, n_s, k_{\text{min}}, k_{\text{max}})$ is fixed. While for the analysis in Section V B, we consider the clustering factor R_{cl} appearing in Eq. (24) as an extra free parameter in addition to the primordial spectrum parameters, such that the total GWB is now given by $\Omega_{\text{gw}}(f; R_{\text{cl}}, A_\zeta, n_s, k_{\text{min}}, k_{\text{max}})$. This allows us to consider models with enhanced PBH clustering. Here, we also include a scenario where the entire GW background arises from PBH binaries only.

A. Fixed Clustering Factor Analysis

In this first analysis, the clustering factor R_{cl} multiplying the late PBH merger rate in Eq. (24), is computed using the PBH halo mass function including Poissonian fluctuations (Eq. (C15)) for fixed primordial power spectrum parameters. The total GW spectrum in Eq. (30) is only a function of the primordial parameters, $\Omega_{\text{gw}} \equiv \Omega_{\text{gw}}(f; A_\zeta, n_s, k_{\text{min}}, k_{\text{max}})$.

We derive the posterior distributions of the primordial parameters $A_\zeta, n_s, k_{\text{min}}, k_{\text{max}}$ after setting logarithmic uniform priors for $A_\zeta, k_{\text{min}}, k_{\text{max}}$ and uniform prior for the spectral index n_s , with prior limits given in Table II. We furthermore restrict our analysis to the parameter space constrained by $f_{\text{PBH}} \leq 1$ and where the primordial power spectrum respects the known constraint from the CMB μ -distortion [56] (see Appendix. D).

The one- and two-dimensional posterior distributions for the fixed R_{cl} analysis are shown in blue in Fig. 4, where the light and dark regions represent 95 % and 68 % C.I. regions respectively. The maximum posterior values and the 68 % C.I. for the curvature amplitude are given by $\log_{10} A_\zeta = -2.06 \in [-2.20, -1.99]$, while for the spectral index are given by $n_s = 0.97 \in [0.83, 1.14]$. From the full posterior distributions shown in Fig. 8, we can see the maximum posterior values for the cut-off scales in the primordial spectrum: $\log_{10} k_{\text{min}}/\text{Mpc}^{-1} = 5.68 \in [4.62, -]$ (where the upper 68% limit does not exist), $\log_{10} k_{\text{max}}/\text{Mpc}^{-1} = 7.33 \in [6.73, 12.42]$.

For these maximum posterior values (see also Fig. 4), the PTA signal is always dominated by the scalar induced GWB, $\Omega_{\text{gw}}^{\text{SIGGW}}(f)$ with the PBH binaries giving a much sub-leading contribution to the total GW spectrum. To explain the PTA common-spectrum process, a spectral index $n_s \sim 1.3$ would yield the required increasing frequency dependence of the GW spectrum from SIGWs, $\Omega_{\text{gw}}^{\text{SIGGW}} \propto f^{2(n_s-1)}$. With the amplitude fixed at $A_\zeta \sim 10^{-2}$ and $k_{\text{max}} \sim 10^7 \text{ Mpc}^{-1}$, a resulting signal of $\Omega_{\text{gw}} \sim \mathcal{O}(10^{-9})$, covering the highest PTA frequency bin $f_{\text{max}} \sim 10^{-8} \text{ Hz}$ can be obtained. However, for these parameter values, light PBHs will overclose the Universe giving $f_{\text{PBH}} \geq 1$. This explains the preferred central values we obtain for the spectral index $n_s \sim 0.97$. This n_s

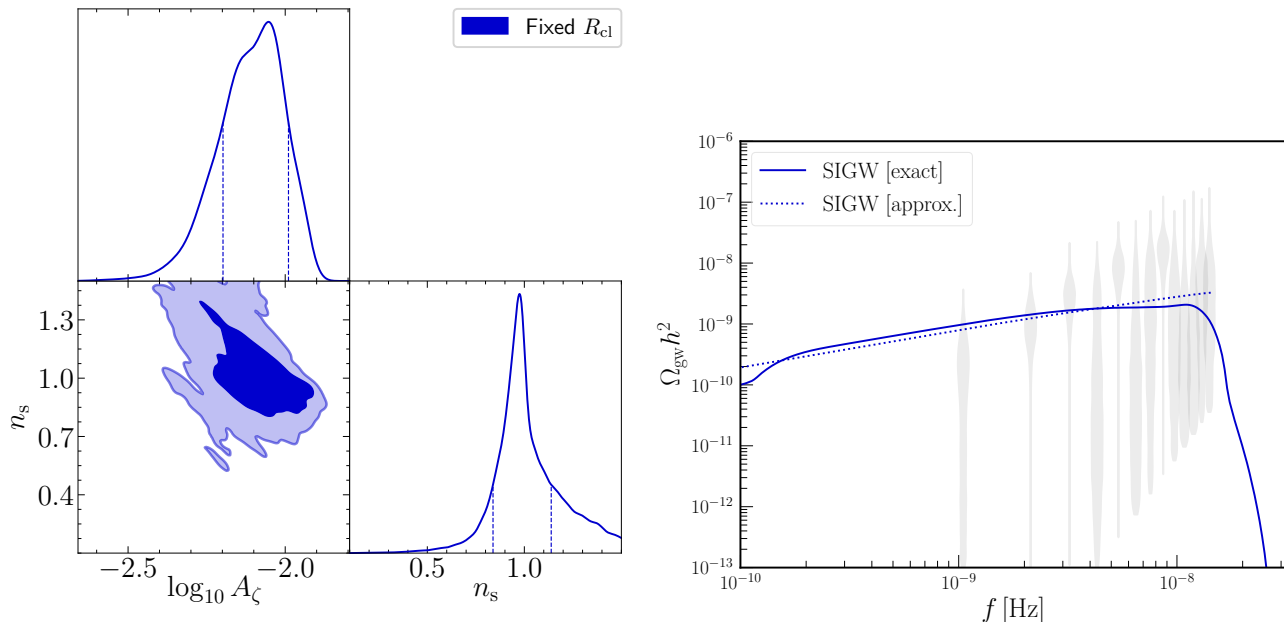


FIG. 4. *Left:* Posterior distributions for the parameters A_ζ and n_s of the primordial power spectrum defined in Eq. (3) for the fixed clustering analysis (blue). The 1d marginalized distributions are reported on the diagonal of the corner plot, with the 68 % Bayesian credible intervals (vertical lines), while the off-diagonal panel (2d distribution) shows the 68 % (darker) and 95 % (lighter) C.I. regions respectively. The posteriors shown respect $f_{\text{PBH}} \leq 1$ as well as the CMB μ distortion limits from FIRAS/COBE [96, 97]. *Right:* GW spectrum obtained for the maximum likelihood values of parameters ($\log_{10} A_\zeta = -2.11$, $n_s = 1.31$, $\log_{10} k_{\text{min}} = 4.80$, $\log_{10} k_{\text{max}} = 6.96$) for the fixed R_{cl} analysis, containing contribution only from scalar induced GWs (see main text). Gray violins shown indicate the free spectrum posteriors obtained by converting the results of IPTA DR2 [33].

value results in a broad PBH mass distribution, where k_{max} is not restricted by the $f_{\text{PBH}} \leq 1$ constraint. This can be further seen in the 2d distribution for (n_s, k_{max}) in Fig. 8, where for $n_s \sim 1$, all $k_{\text{max}}(k_{\text{min}})$ values are allowed. Additionally, the CMB μ -distortion limit becomes important for $\log_{10} k_{\text{min}} \lesssim 4.4$, which explains the cut-off in the corresponding 2d distribution for $(n_s, \log_{10} k_{\text{min}})$. Finally, the upper limit on the curvature perturbation amplitude of $\log_{10} A_\zeta \leq -1.9$ is set by the $f_{\text{PBH}} \leq 1$ constraint. The resulting maximum likelihood GW spectrum for this analysis is shown Fig. 4 (right) as solid (dotted) curves for the exact (approximate) GWB arising from the dominant scalar induced GW component obtained using Eq. (10) (Eq. (13)).

The PBH binaries in this analysis give a sub-leading contribution to the total GW spectrum as already mentioned. This can be understood as follows: the typical value of the clustering factor, R_{cl} , from Eq. (C15), is approximately $\mathcal{O}(1 - 100) \text{ Gpc}^{-3} \text{ yr}^{-1}$ for mass distributions with $n_s \lesssim 1$ (see also Fig. 3). In contrast, for mass spectra with $n_s > 1$, the clustering parameter can be large $R_{\text{cl}} \sim 10^6 \text{ Gpc}^{-3} \text{ yr}^{-1}$ (see also Fig. 3), however, for these values of n_s , the average PBH mass is typically $\ll 1 M_\odot$ for $k_{\text{max}} > 10^7 \text{ Mpc}^{-1}$, leading to an overall small merger rate from late PBH binaries. Moreover, the CMB μ -distortion limits set $k_{\text{min}} \gtrsim 10^{4.4} \text{ Mpc}^{-1}$ which corresponds to a cut-off in the PBH mass function giving

$m \lesssim 1000 M_\odot$, resulting in a significant suppression of the late-time PBH merger rate in Eq. (24). Consequently, the GW spectrum from PBH binaries, $\Omega_{\text{gw}}^{\text{PBHB}}(f)$, is suppressed at nHz frequencies.

Finally, we compare this PBH model with a fixed clustering factor to the astrophysical model of inspiralling SMBHBs. The GW background for the latter is characterized by a power-law given by

$$\Omega_{\text{gw}}^{\text{SMBHB}} = \frac{2\pi^2}{3H_0^2} A_{\text{BHB}}^2 \left(\frac{f}{\text{yr}^{-1}} \right)^{5-\gamma_{\text{BHB}}} \text{yr}^{-2}, \quad (31)$$

where we have fixed $\gamma_{\text{BHB}} = 13/3$ [108] and varied the amplitude A_{BHB} , with log uniform priors for the latter given by $-18 \leq \log_{10} A_{\text{BHB}} \leq -11$.

Search	Bayes Factors
SIGWs + PBHBs [Fixed R_{cl}]	$\log_{10}(B_{\text{SMBHB,PBH}}) = 1.88$
SIGWs + PBHBs [Free R_{cl}]	$\log_{10}(B_{\text{SMBHB,PBH}}) = 1.86$
PBHBs [Free R_{cl}]	$\log_{10}(B_{\text{SMBHB,PBH}}) = 0.05$

TABLE I. Summary table for Bayes factors $B_{\text{SMBHB,PBH}}$ for the astrophysical SMBHB model with respect to the PBH model for the free and fixed clustering factor analyses.

We compare the two models using the Bayes factor, $\log_{10} B_{a,b}$, of model a with respect to model b . With the IPTA DR2 analysis for fixed R_{cl} (see Fig. 4), we find: $\log_{10}(B_{\text{SMBHB,PBH}}) \simeq 2$ (see Table I), which implies very strong evidence for the astrophysical SMBHB model over the PBH merger model with fixed clustering parameter R_{cl} including SIGWs triggered at PBH formation.

B. Free Clustering Factor Analysis

In this section, we describe the analysis in which the clustering factor R_{cl} in the PBH merger rate (in PBH clusters) in Eq. (24) is considered to be a free parameter. The total GW spectrum in Eq. (30) also depends on the clustering parameter now i.e., $\Omega_{\text{gw}} \equiv \Omega_{\text{gw}}(f; A_{\zeta}, n_s, k_{\text{min}}, k_{\text{max}}, R_{\text{cl}})$. This can help determine the enhancement in late-time PBH merger rates required to fit the PTA signal, and verify whether such large PBH merger rates can be realistic and accounted for with current uncertainties on the PBH clustering model (described in appendix C 4).

We consider a uniform logarithmic prior on the free clustering parameter: $\log_{10} R_{\text{cl}} \in [0, 10]$ (see also Table II). The μ -distortion limits from COBE/FIRAS [56] and $f_{\text{PBH}} \leq 1$ constraint are implemented as before.

The one- and two-dimensional posterior distributions for the free R_{cl} analysis including both contributions from SIGWs and PBH binaries to the GWB are shown in blue in Fig. 5 (full posteriors shown in Fig. 9). The maximum posterior values and the 68 % C.I. for the curvature amplitude is given by $\log_{10} A_{\zeta} = -2.10 \in [-2.28, -1.97]$. For the spectral index, the maximum posterior value is given by $n_s = 0.97$ and the 68 % C.I. upper limit is $n_s < 1.22$ (no lower limit exists). The free clustering parameter reaches the maximum posterior value at $\log_{10} R_{\text{cl}}/\text{Gpc}^{-3}\text{yr}^{-1} = 10$, (equal to the upper limit of the prior value) with the 68 % C.I. lower limit given by $\log_{10} R_{\text{cl}}/\text{Gpc}^{-3}\text{yr}^{-1} > 4.10$. From the full posterior distributions shown in Fig. 9 (in blue), the maximum posterior values and the 68 % C.I. for the cut-off scales in the primordial spectrum are: $\log_{10} k_{\text{min}}/\text{Mpc}^{-1} = 4.58 \in [4.39, 5.91]$, $\log_{10} k_{\text{max}}/\text{Mpc}^{-1} = 6.99 \in [6.69, 13.89]$. For these maximum posterior values, the GW spectrum is dominated by the scalar induced GWs and the contribution from (late) PBH binaries to the GW spectrum at $f \sim 1$ nHz, is very suppressed, $\Omega_{\text{gw}}^{\text{PBHB}} \sim 10^{-17}$.

The 2-d posterior distribution for (A_{ζ}, n_s) shows two distinct regions in Fig. 5 (left). The region with larger values of spectral index ($n_s \geq 0.8$) corresponds to the parameter space for which the PTA signal is dominated by GWB from SIGWs. This can be seen from the 2-d posterior distribution of (R_{cl}, n_s) in (left) Fig. 5 where for $n_s \sim 1$, all values of R_{cl} are allowed. Whereas, the second region with lower values of the spectral index ($n_s \leq 0.8$) corresponds to a PTA signal fitted by a GWB contribution from both scalar induced GWs and PBH binaries. The clustering factor required to enhance the contribu-

tion from late PBH binaries is $R_{\text{cl}} \geq 10^4 \text{ Gpc}^{-3} \text{ yr}^{-1}$, much larger than the expected value for Poisson fluctuation induced PBH clustering (see typical values in Fig. 3). Moreover, the late PBH binaries in this analysis can only contribute to the total GWB when $R_{\text{cl}} f_{\text{PBH}}^2 \sim \mathcal{O}(1)$. This can explain the large maximum posterior value of clustering factor, $R_{\text{cl}} \sim 10^{10} \text{ Gpc}^{-3}\text{yr}^{-1}$ obtained, which compensates for the small f_{PBH} values. Since $\Omega_{\text{gw}}^{\text{PBHB}} \propto f_{\text{PBH}}^2$ for late PBH binaries, changing $\log_{10} A_{\zeta}$ even slightly leads to a drastic change in the GW contribution from late binaries, whereas the scalar induced spectrum remains almost constant due to the quadratic dependence on the power spectrum amplitude $\Omega_{\text{gw}}^{\text{SIGW}} \propto A_{\zeta}^2$.

The resulting maximum likelihood GW spectrum for this analysis is shown Fig. 5 (right) where the total GW background is a combination from scalar induced (shown in blue solid) till the cut-off $k_{\text{max}}(f_{\text{max}}) \sim 10^7 \text{ Mpc}^{-1} (10^{-8} \text{ Hz})$. For the higher frequency bins $f > f_{\text{max}}$, the PTA signal is fitted with the contribution from (late) PBH binaries (shown in dashed red). A strong preference is found in favor of the astrophysical model with only inspiralling SMBHBs in comparison to this PBH model with SGWB from PBH binaries and associated SIGWs, with the Bayes factor $\log_{10}(B_{\text{SMBHB,PBH}}) = 1.86$.

Finally, a similar analysis is performed with the free R_{cl} parameter including the contribution from PBH binaries (late and early) only (without the SIGWs contribution). The 1d, 2d posterior distributions are shown in the left panel of Fig. 5 in yellow. The maximum posterior values for all parameters and the corresponding 68 % C.I. are: $\log_{10} A_{\zeta} = -1.971 \in [-2.11, -1.78]$, $n_s = 0.72 \in [0.16, 0.88]$, $\log_{10} R_{\text{cl}}/\text{Gpc}^{-3}\text{yr}^{-1} = 10$ (equal to the upper prior limit) with the lower 68 % limit given by $\log_{10} R_{\text{cl}}/\text{Gpc}^{-3}\text{yr}^{-1} \geq 6.87$. From the full posteriors shown in Fig. 9 (in yellow), the maximum posterior values for the cut-off scales in the spectrum are: $\log_{10} k_{\text{min}}/\text{Mpc}^{-1} = 4.91 \in [4.54, 5.48]$ and $\log_{10} k_{\text{max}}/\text{Mpc}^{-1} = 6.48 \in [6.05, 17.83]$. Since in our model, the R_{cl} parameter enters only in the late binary GWB, the only dominant contribution comes from the late PBH binary channel. The total PBH abundance f_{PBH} for these maximum posterior values is 0.1 and for a large range of PBH masses, the posterior PBH abundance is strongly constrained from CMB (see Fig. 6 in the next section and the related explanation).

VI. PBH CONSTRAINTS

In this section, we describe the constraints on the PBH $(f_{\text{PBH}}(m), m)$ parameter space obtained from our analysis with IPTA DR2 in relation to existing PBH constraints. Fig. 6 shows the posterior predictive distribution for the PBH abundance $f_{\text{PBH}}(m)$ (as defined in

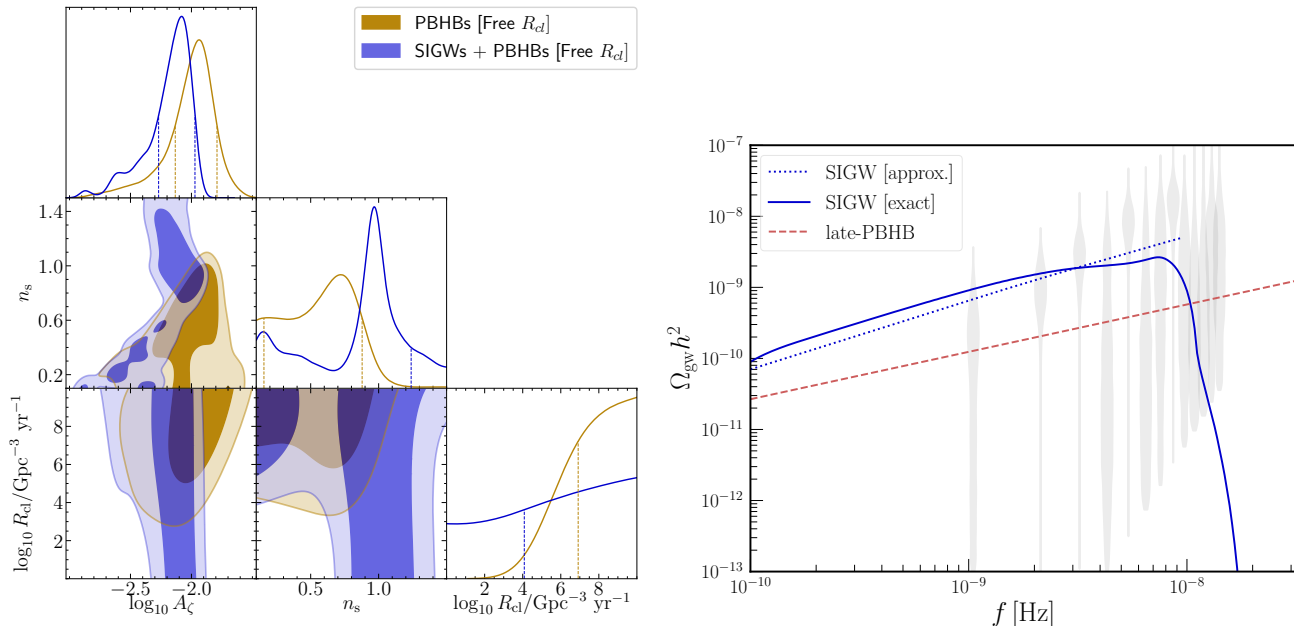


FIG. 5. *Left*: Posterior distributions for the parameters of the primordial power spectrum defined in Eq.(3) for the free clustering parameter R_{cl} analysis. The 1d marginalized distributions are reported on the diagonal of the corner plot while the off-diagonal panel (2d distribution) shows the 68 % (darker) and 95 % (lighter) C.I. regions respectively. The blue and yellow contours correspond respectively to the analyses performed with SIGWs + PBH binaries and with PBH binaries only. *Right*: Maximum likelihood GW spectrum for the free clustering analysis ($\log_{10} A_\zeta = -2.11$, $n_s = 1.49$, $\log_{10} k_{\min} = 4.61$, $\log_{10} k_{\max} = 6.78$) with contribution from both SIGWs and late PBH binaries. The signal is dominated at small frequencies by the SIGWs (blue), scaling as $\Omega_{\text{gw}}^{\text{SIGW}} \sim f^{2(n_s-1)}$, and from $f > f_{\max} \sim 10^{-8}$ Hz onwards, by GWB from inspiralling (late) PBH binaries (dashed red) with the characteristic scaling $\Omega_{\text{gw}}^{\text{PBHB}} \sim f^{2/3}$.

Eq. (7)) obtained from the PTA inference, alongside the most stringent existing constraints (see Ref. [13] for a recent review on this) in this PBH mass range.

In the planetary-mass and low stellar-mass range up to $m \sim 10 M_\odot$, the strongest constraints on the PBH abundance $f_{\text{PBH}}(m)$ come from microlensing surveys. These include: EROS searches for massive compact halo objects (MACHOs) towards the Large Magellanic Cloud (LMC) [118], fast transient event (ICARUS) near critical curves of massive clusters [119, 120], and the most recent results from observation of stars in LMC and Galactic Bulge by the Optical Gravitational Lensing Experiment (OGLE) [121]. In the stellar and intermediate mass ranges, the most stringent limits come from X-ray emissions from PBHs interacting with the interstellar medium. In Fig. 6, we show bounds coming from observation of X-ray binaries [122], cosmic radio and cosmic X-ray backgrounds from ARCADE2 and Chandra [123]. More stringent limits from LVK black hole population analysis [124] exist but they do not apply to our mass distributions with $n_s \gtrsim 0.9$.

In the intermediate mass range, the most severe constraints are coming from CMB anisotropies produced by accreting PBHs in the early Universe, where we are showing the bounds from Ref. [125]. Note that in general bounds on PBHs from CMB anisotropies can change

drastically on changing the PBH accretion model and on including DM mini-halos, and they additionally suffer from astrophysical uncertainties. Ref. [126] set a conservative limit on PBHs from CMB where for $2M_\odot \lesssim m \lesssim 10^4 M_\odot$, the PBH abundance is constrained to be $10^{-3} \lesssim f_{\text{PBH}} \lesssim 1$ (see also Ref. [127]). Finally, we have shown dynamical limits coming from the distribution of stars in Segue I [128] and Eriadnus II [53] dwarf galaxies in Fig. 6.

The predictive PBH abundance distributions shown in Fig. 6 correspond to the PBH mass distributions for the maximum posterior parameter values obtained from the Bayesian inference of the IPTA DR2. In Fig. 6 the solid red curve corresponds to the scenario where only late-time PBH binaries contribute to the entire GWB and the clustering parameter, R_{cl} , is free. The dark blue (yellow) curves correspond to the scenario where all channels, SIGWs, early PBHBs and late PBHBs, are included in the GWB analysis for free (fixed) clustering parameter R_{cl} , respectively. We observe that the distribution obtained for only PBH binaries with free R_{cl} is excluded by several probes, including the most conservative CMB limits. Moreover, the posterior values for this analysis give $f_{\text{PBH}} \sim 0.8$, $\langle m \rangle \sim 600 M_\odot$, and are in violation of the constraints coming from LVK merger rates $\sim \mathcal{O}(1 - 100) \text{ Gpc}^{-3} \text{yr}^{-1}$ [129].

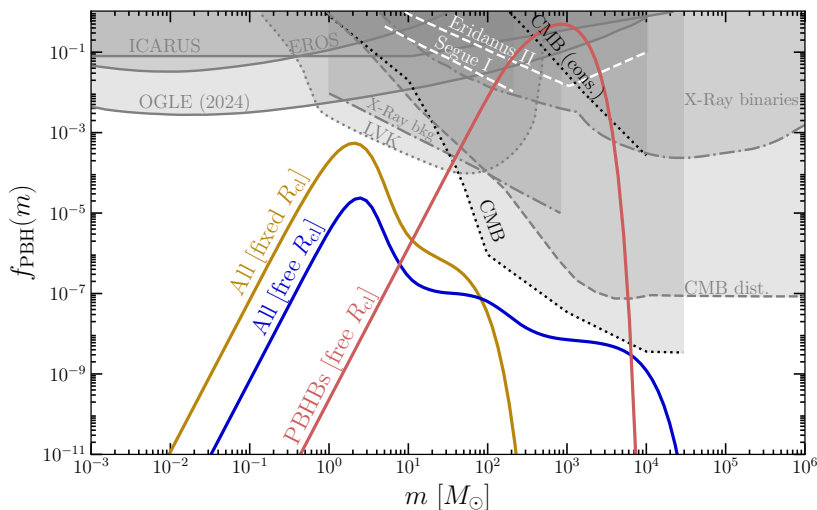


FIG. 6. The PBH mass distribution derived using the maximum posterior values of our model parameters obtained from the PTA inference this work, compared to existing (most stringent) constraints on PBHs [23]. Among existing PBH constraints, we have shown microlensing ones from EROS [118], ICARUS [119] and OGLE [121] (solid gray), dynamical limits from the heating of dwarf galaxies Eridanus II and Segue I (white dashed), constraints from X-ray binaries [122] and X-ray background (dot-dashed gray) [X-ray bkg] and finally constraints coming from CMB distortions [CMB dist.] (gray dashed) as well as the most stringent [125] [CMB] and conservative constraints [126] [CMB (cons.)] from CMB anisotropies (dotted black). Constraints from Ligo-Virgo-KAGRA O3 merger rates (dotted gray) shown here have been taken from Ref. [124].

The two other analyses including SIGWs, however, evade all these limits and are viable. The posterior values for the fixed and free R_{cl} analysis, including the contribution from both SIGWs and PBH binaries to the GWB, peak at $f_{PBH} \sim 10^{-5} - 10^{-4}$, at PBH mass of around $4 - 10 M_{\odot}$. Moreover, the merger rates of both early and late PBH binaries in these two scenarios are compatible with the LVK constraints for merger rates (see also Ref. [124]). This can open some interesting perspectives for PBH models to explain at the same time a small fraction of LVK mergers and the GWB observed by PTAs.

VII. CONCLUSION AND DISCUSSION

In this work, we have searched for a GW background arising from inspiralling PBH binaries in the International PTA dataset (IPTA DR2). We have considered two channels for PBH binary formation in our analysis: PBH pair formation in the early Universe as well as PBH binary formation via dynamical capture in late-Universe PBH clusters. While for small PBH abundance or f_{PBH} , PBH binaries decoupled in the early Universe from the Hubble flow can dominate the merger rate, for large values of f_{PBH} , PBH binaries formed dynamically inside PBH clusters can be dominant. Our Bayesian search in the IPTA DR2 was largely motivated by the results of Ref. [55] which showed that a GWB from late-time PBH binaries could be large enough to be probed by PTAs at the nHz frequency range, due to a large contribution from binaries with asymmetric masses (between a solar-mass PBH and an intermediate-mass PBH).

Our analysis shows that such a contribution to the GWB is largely suppressed due to the need to introduce a cut-off at scale $k_{min} \sim 10^5 \text{ Mpc}^{-1}$ to evade the limits from CMB μ -distortions [56], which restricts the formation of PBH with mass $m \gtrsim 1000 M_{\odot}$.

In comparison to previous works, our analysis is based on merger rates for a broad PBH mass function including the features from the QCD epoch (as detailed in sec. II). The broad PBH mass function used in our analysis has been derived assuming the direct collapse of enhanced density perturbations obtained from a power-law power spectrum of curvature perturbations at small scales, with a large-mass cut-off (or small k , k_{min}) introduced to evade the constraints from CMB μ -distortions and a low-mass cut-off (or large k , k_{max}) to prevent overclosing the Universe with light PBHs. Most importantly in relation to previous works, in our analysis for the search for GWB from PBH binaries, we have included the scalar induced stochastic GW background, which will be unavoidable due to the enhanced curvature perturbations needed for PBH formation in the standard scenario.

We also note some limitations in our computation for merger rates both from early binaries and late binaries. For broad PBH mass spectra obtained for $n_s \sim 0.96$, the early merger rate suppression from third-PBHs is still uncertain [55]. For the late PBH binaries, we have carefully accounted for the formation of PBH binaries in late small scale halos with the correct halo mass function for Poissonian fluctuations, and included effects from dynamical heating [53, 54] on the cluster size. Both these effects, as we also discuss in Appendix C4, can have an important impact on the late merger rates. This latter effect of

dynamical heating, in addition to, effects of mass segregation between light PBHs and heavy PBHs can lead to uncertainties on the late merger rate computation for broad PBH mass distribution (obtained for $n_s \sim 1$). Our work, nevertheless, provides a rigorous and complete template for merger rate computation that can be used for analysis involving PBH merger rates, for instance for analysing limits on the GW background by LIGO-Virgo-Kagra.

Our main results from the Bayesian inference show that the contribution to the GWB from PBH binaries (both early and late channels) is largely subdominant with respect to the GWB from scalar induced perturbations for power law PBH mass distributions (see Sec. V A). It is not possible to explain the PTA signal with only PBH binaries in late time PBH clusters, under the assumption of standard PBH formation scenario with PBH clustering from Poissonian fluctuations.

We further performed an analysis with a nuisance parameter in the PBH merger rate from late binaries given by the “free” clustering parameter R_{cl} (see Sec. V B). We find that the values of R_{cl} required to explain the PTA signal with late PBH binaries is $\sim \mathcal{O}(10^4)$ Gpc $^{-3}$ yr $^{-1}$ larger than the R_{cl} values arising from Poissonian fluctuations. Nevertheless, this analysis with the free clustering parameter R_{cl} can serve as a proxy for the enhancement in PBH clustering required for the GWB from late PBH binaries to dominate over the SIGW background. An enhancement in PBH clustering will necessarily impact the early PBH binary merger rates as well (see Refs. [58–60]). However, our analysis, which uses a free clustering parameter, neglects this effect in the early PBH merger rate as it is difficult to estimate.

Our analysis also reveals that PBH mass distributions with $n_s \lesssim 1$ are statistically preferred, because they naturally suppress low-mass PBHs (from overclosing the Universe) and do not require a small-scale cut-off k_{max} .

In addition to the two channels considered in our analysis, a third channel via three-body interaction can also lead to PBH binary assembly in small scale PBH halos. Ref. [130] has shown that this can give a larger contribution than the capture channel in small clusters. Given the required enhancement of merger rates to match the PTA signal, it is unlikely that the inclusion of this channel will have an impact on our main conclusions. Additionally, we always consider non-eccentric or circular binaries. The dynamical channel for PBH binary formation can lead to highly eccentric binaries as shown in Ref. [131]. A more detailed analysis comparing all channels and incorporating eccentric binaries is left for a future work.

In some sense, our analysis in this work contributes to the search for the cosmological origin of the PTA signal by excluding a series of plausible scenarios related to PBHs. As a corollary of our analysis, we can identify the following scenarios that can possibly lead to an increase in the merger rates from PBH binaries in the late-Universe: an increased clustering at PBH formation could lead to an increased merger rates from both early

PBH binaries as well as late-time dynamically formed PBH binaries. In addition, an effect opposing the dynamical heating leading to contraction of the PBH cluster radius (such as gravitational cooling) could also enhance the merger rate. Note that such such enhanced PBH clustering could also have a significant effect on the microlensing constraints on PBH abundance (see for example Ref. [132]). While for PBH formation from Gaussian perturbations, clustering at PBH formation is negligible, for non-Gaussian perturbations, an enhanced clustering can be expected as shown in Ref. [133].

Moreover, in order to form PBHs with mass $m \gtrsim 1000 M_\odot$, which can eventually lead to increased merger rates and subsequently a larger GWB, a PBH formation mechanism is required that can evade the tight CMB spectral distortion limits on the primordial perturbation amplitude at scales larger than $k \sim 10^5$ Mpc $^{-1}$. While in general, it is very challenging to form massive PBHs from direct collapse, these limits can be avoided, if the distribution of primordial curvature perturbations is highly non-Gaussian [134]. Under this mechanism, PBHs can form from the smaller peaks in the primordial power spectrum from the tail of a sufficiently non-Gaussian distribution of the curvature perturbations ζ . While, large scale observations on non-Gaussianity parameters f_{NL} and g_{NL} constrain ζ to be nearly Gaussian [135], small scales related to PBH formation are free from such constrains. See recent work in Ref. [136] on the formation of super-massive PBHs from non-Gaussian ζ .

An additional possible route to evade CMB spectral distortion limits that can additionally suppress the GWB from SIGWs is to consider another PBH formation mechanism such as PBHs produced from a first-order phase transition [8].

In addition to μ -distortion limits, our results are also strongly dependent on the condition that PBHs do not overclose the Universe, $f_{PBH} \leq 1$. Indeed, we have implemented this condition in obtaining our final posteriors shown in Sec. V and App. F. Since the computation for PBH abundance is exponentially sensitive to the choice of the window function, the threshold for PBH formation (see also discussion in Ref. [48]) and to the method of abundance computation, our posterior parameter values are subject to this theoretical uncertainty as well.

In the next few years, the combined dataset from all PTAs will be released as International PTA Data Release 3 (IPTA DR3), the analysis of which will improve our understanding on the origin of the GW excess in the nHz frequency range. While the most plausible motivation for this excess comes from astrophysical SMBHBs, as has been shown in literature, the origin of this signal can arise also from many well-motivated new physics scenarios in the early Universe. Our work clarifies the premises and assumptions that would be needed to see a GW background from PBH mergers in the dataset.

ACKNOWLEDGMENTS

We would like to thank members of the IPTA and NANOGrav collaborations for useful comments on a preliminary version of this work. SV would also like to thank G. Franciolini, G. Domènech, S. Babak for useful discussions and comments. The work of SV is supported by the Excellence of Science (EoS) project No. 30820817 - be.h “The H boson gateway to physics beyond the Standard Model” and by the IISN convention 4.4503.15. The work of S.C. is supported by an Incentive Grant for Scientific Research (MIS) from the Belgian Fund for Research FNRS, and by the IISN convention 4.4501.19.

Appendix A: Scalar Induced GWs

In this appendix, we provide the analytical expressions that are used to calculate the GW spectrum during the radiation era. It is obtained by solving the double integral

$$\Omega_{\text{gw, RD}}(k, \eta) = \frac{1}{12} \left(\frac{k}{a(\eta)H(\eta)} \right)^2 \int_0^\infty dt \int_{-1}^1 ds \times \left[\frac{t(2+t)(s^2-1)}{(1-s+t)(1+s+t)} \right]^2 I_{\text{RD}}^2(u, v, k\eta) \mathcal{P}_\zeta(uk) \mathcal{P}_\zeta(vk), \quad (\text{A1})$$

with $H(\eta)$, $a(\eta)$ being the Hubble rate and the scale factor as a function of the conformal time η . An additional time dependence is contained inside the function $I_{\text{RD}}(u, v, k\eta)$. In the limit $k\eta \gg 1$, it is given by [26]

$$I_{\text{RD}}(u, v, x \rightarrow \infty) = \frac{1}{x} \left(\frac{3(u^2 + v^2 - 3)}{4u^3v^3} \right) \left(\sin(x) \left(-4uv + (u^2 + v^2 - 3) \log \frac{|3 - (u+v)|}{|3 - (u-v)|} \right) - \pi(u^2 + v^2 - 3)\Theta(v + u - \sqrt{3}) \cos(x) \right). \quad (\text{A2})$$

For the production of SIGWs from small scales primordial perturbations, it is reasonable to assume that all the relevant modes k enter the horizon early in radiation domination. Hence, deep in radiation domination, those modes satisfy the condition $k\eta \gg 1$. On taking the oscillation average after squaring Eq. (A2) above, the factors of $\sin^2(x)$ and $\cos^2(x)$ will simply give a factor of $1/2$. We can thus write the oscillation average as:

$$\bar{I}_{\text{RD}}^2(u, v, x) = \frac{1}{2x^2} \left(\frac{3(u^2 + v^2 - 3)}{4u^3v^3} \right)^2 \left(\left(-4uv + (u^2 + v^2 - 3) \log \frac{|3 - (u+v)|}{|3 - (u-v)|} \right)^2 + \pi^2(u^2 + v^2 - 3)\Theta(v + u - \sqrt{3}) \right). \quad (\text{A3})$$

One can note that the time dependence in the pre-factor of Eq. (A1), $k/(aH) = k\eta = x$, cancels the time dependence of $\bar{I}_{\text{RD}}^2(u, v, x)$ encoded in x^{-2} in Eq. (A3). The GW spectrum in the radiation era is therefore time-independent, as expected since GWs scale as radiation $\rho_{\text{GW}} \propto \rho_r \propto a^{-4}$.

Appendix B: Thermal average of binary cross-section

In this appendix, we give details on how to compute the thermal average of the binary-formation cross-section defined in Eq. (19).

As mentioned in the main text, following the velocity model of Ref. [102], one can approximate the PBH relative velocity denoted by v with a Maxwell-Boltzmann distribution

$$P(v) = N \left[\exp\left(-\frac{v^2}{v_{\text{esc}}^2}\right) - \exp\left(-\frac{v_{\text{vir}}^2}{v_{\text{esc}}^2}\right) \right], \quad (\text{B1})$$

where the second term in the distribution introduces a cut-off at the virial velocity of the halo, defined as

$$v_{\text{vir}} \simeq \sqrt{\frac{GM_{\text{h}}}{r_{\text{h}}}}, \quad (\text{B2})$$

while N is a normalisation constant found by imposing $\int_0^{v_{\text{vir}}} d^3v P(v) = 1$. Here, v_{esc} is the PBH velocity dispersion in the halo, defined as the escape velocity at the radius $R_{\text{max}} = C_{\text{m}}R_{\text{s}}$ with $C_{\text{m}} = 2.1626$,

$$v_{\text{esc}} = \sqrt{\frac{GM(R < R_{\text{max}})}{R_{\text{max}}}} = v_{\text{vir}} \sqrt{\frac{C}{C_{\text{m}}} \frac{g(C_{\text{m}})}{g(C)}}, \quad (\text{B3})$$

where $g(C_{\text{m}}) = 0.46759$ and

$$M(R < R_{\text{max}}) = \int_0^{R_{\text{max}}} 4\pi r^2 \rho_{\text{NFW}}(r) dr. \quad (\text{B4})$$

Using Eq. (B1), we can finally compute the thermal average of the cross-section as

$$\begin{aligned} \langle \sigma_{\text{bin}} v \rangle &= 4\pi \int_0^{v_{\text{vir}}} dv \sigma_{\text{bin}} v^3 P(v) \\ &= 2\pi \left(\frac{85\pi}{6\sqrt{2}} \right)^{2/7} \frac{G^2(m_1 + m_2)^{10/7} (m_1 m_2)^{2/7}}{c^{10/7}} \\ &\quad \times v_{\text{vir}}^{-11/7} \mathcal{F}[C_{\text{m}}, C(M_{\text{h}}), g(C_{\text{m}}), g(C)] \end{aligned} \quad (\text{B6})$$

where σ_{bin} is given by Eq. (19) and where $\mathcal{F}[C_{\text{m}}, C(M_{\text{c}}), g(C_{\text{m}}), g(C)] \equiv \mathcal{F}_{\text{avg}}$ is a complicated function of the parameters C_{m} and C that remains after the integration of the Maxwellian velocity distribution given in Eq. (B1). To a very good approximation, $\langle \sigma_{\text{bin}} v \rangle \approx 3 \sigma_{\text{bin}}(v_{\text{vir}}) v_{\text{vir}}$. Note that, picking any other velocity distribution could lead to a larger thermal average. This uncertainty from the choice of the PBH velocity distribution will be captured by our free R_{cl} clustering analysis (see section VB).

Appendix C: PBH Clustering

In this appendix, we discuss the Poisson fluctuations in the PBH number density that contribute as an additional term in the matter power spectrum, dominant at small scales. As mentioned in the main text, within the Press-Schechter formalism, these fluctuations collapse and form PBH halos. We first provide a calculation of the clustering factor introduced in Eq. (24), resulting from this effect. Then we discuss the dynamical heating of PBH clusters to obtain the minimum cluster mass M_{\min} .

1. Poisson fluctuations from PBHs

Due to the discrete nature of PBHs, Poisson fluctuations are expected in their local number density [92]. These Poisson fluctuations give rise to isocurvature perturbations in the matter power spectrum that could be observable as a small-scale plateau [137] (see also e.g. Refs. [54, 93, 138–140] for analyses including Poisson fluctuation effects for PBH dark matter). We have neglected other possible sources of isocurvature fluctuations and particle dark matter clustering.

The cold dark matter power spectrum $P_{\text{CDM}}(k)$ ⁸ in our scenario is therefore the sum of contributions from the adiabatic perturbations and isocurvature perturbations originating from these Poisson fluctuations. The adiabatic perturbations include the standard contribution from the primordial power spectrum on large scales and the small-scale term introduced in Eq. 3. The additional isocurvature contribution expected from Poisson fluctuations, in the case of a monochromatic PBH distribution, is given by [91, 93],

$$P_{\text{iso}}^{\text{PBH}} = f_{\text{PBH}}^2 n_{\text{PBH}}^{-1} D_{\text{PBH}}^2(z) \quad (\text{C1})$$

$$\simeq 1.7 \times 10^{-3} f_{\text{PBH}} \left(\frac{m}{3 M_{\odot}} \right) (1+z)^{-2} \text{Mpc}^3,$$

where $D_{\text{PBH}}(z)$ is the growth factor of PBH induced perturbations that can be approximated analytically as [93]

$$D_{\text{PBH}}(z) = \left(1 + \frac{3}{2} \frac{\Omega_{\text{DM}}}{\Omega_{\text{m}}} \frac{1+z_{\text{eq}}}{1+z} \right) \quad (\text{C2})$$

where $z_{\text{eq}} \approx 3400$ is the redshift for matter-radiation equality, n_{PBH} is the average number density of PBHs in a comoving volume and we have used $n_{\text{PBH}} m = f_{\text{PBH}} \Omega_{\text{DM}}^0 \rho_c$ in the second line in Eq. (C1), with $\Omega_{\text{DM}}^0 = 0.265$, $\rho_c = 2.77 \times 10^{11} h^2 M_{\odot} \text{Mpc}^{-3}$ and $h = 0.674$. Note that the above equation holds only for $k > k_{\text{eq}}$, which is fulfilled for realistic PBH masses.

⁸ This is the dimensionful matter power spectrum written in terms of the usual dimensionless power spectrum as $\Delta^2 = k^3 P_{\text{CDM}}/2\pi^2$.

In the case of our broad mass distribution, different PBH masses induce Poisson fluctuations and their combined effect requires the substitution of $f_{\text{PBH}} m$ by its averaged value over the considered mass function or $\langle f_{\text{PBH}} m \rangle$ in Eq. C1 [54]. This is given by

$$\langle f_{\text{PBH}} m \rangle = \int m f_{\text{PBH}}(m) d \ln m. \quad (\text{C3})$$

The next step is to use the Press-Schechter formalism to study the mass and size of PBH clusters induced by these Poisson fluctuations.

2. Cluster formation

Here, we give an estimate of the size of the PBH clusters formed from the collapse of Poisson density perturbations. According to the Press-Schechter formalism, the density fluctuations associated to the matter power spectrum, including Eq. (C1), decouple from the Hubble flow and collapse into proper clusters when the overdensity exceeds the critical threshold of $\delta_c \approx 1.686$.

We can write the mass of the cluster contained within a sphere of radius $\lambda = 2\pi/k$ as:

$$M_{\text{h}}(\lambda) = \frac{4\pi}{3} \lambda^3 \rho_{\text{m}}^0 (1+\delta_c) \simeq 2 \times 10^{11} M_{\odot} \left(\frac{\lambda}{\text{Mpc}} \right)^3 (1+\delta_c) \quad (\text{C4})$$

where ρ_{m}^0 is the matter density today. Then a cluster of mass M_{h} , associated to modes for which the Poisson term dominates, will be expected to form around a redshift z_{h} , given by [19]

$$(1+z_{\text{h}}) \simeq 3 \times 10^{-3} \left(\frac{k}{\text{Mpc}^{-1}} \right)^{3/2} \left(\frac{f_{\text{PBH}} m}{M_{\odot}} \right)^{1/2} \quad (\text{C5})$$

$$\simeq 30 \left(\frac{10^6 M_{\odot} \langle m f_{\text{PBH}} \rangle}{M_{\text{h}} M_{\odot}} \right)^{1/2}.$$

To estimate the redshift of cluster formation above, we have used the expectation that at z_{h} , $\Delta_{\text{PBH}}^2 \equiv k^3 P_{\text{iso}}^{\text{PBH}}/2\pi^2 \simeq \delta_c^2$ and used $P_{\text{iso}}^{\text{PBH}}$ defined in Eq. (C1) and further used the cluster mass defined in Eq (C4) associated with k in the second line.

a. Characteristic PBH Halo Mass

In the Press-Schechter formalism, the characteristic PBH halo mass can be defined as the scale at which the PBH overdensity reaches the critical threshold δ_c giving [93]:

$$M_{*}(z) = \frac{2}{\delta_c^2} D_{\text{PBH}}(z)^2 f_{\text{PBH}}^2 m \quad (\text{C6})$$

$$\simeq \frac{2}{\delta_c^2} \cdot \frac{9}{4} \cdot \frac{\Omega_{\text{DM}}}{\Omega_{\text{m}}} \left(\frac{1+z_{\text{eq}}}{1+z} \right)^2 f_{\text{PBH}}^2 m$$

We use this to write Eq. (23), with $f_{\text{PBH}}^2 m$ replaced by $\langle f_{\text{PBH}}^2 m \rangle$, the value averaged over the PBH mass distribution given by:

$$\langle f_{\text{PBH}}^2 m \rangle \equiv f_{\text{PBH}}^2 \int m \phi(m) d \ln m. \quad (\text{C7})$$

b. PBH Cluster Radius

In order to estimate the cluster radius at formation, the spherical collapse theory predicts a cluster density given by $\rho_h \simeq 178 \cdot \rho_c(z = z_h)$ where $\rho_h = 3M_h/(4\pi r_h^3)$. This allows us to write cluster radius, after the cluster has virialized [19],

$$r_h \sim 70 \text{ pc} \left(\frac{\langle m f_{\text{PBH}} \rangle}{M_\odot} \right)^{1/2} \left(\frac{M_h}{10^6 M_\odot} \right)^{5/6}. \quad (\text{C8})$$

where we have used Eq. (C5) and $\rho_c \propto a^{-3}$. Note that in Eqs. (C4), (C5), (C8), we have corrected some numerical factors found in the expressions of [19].

Using the Press-Schechter formalism, we can additionally compute the fraction of fluctuations that will collapse at redshift z_h into PBH halos with a mass M_h using:

$$F(M_h, z_h) = \text{Erfc} \left[\frac{\delta_c}{\sqrt{2}\sigma(M_h, z_h)} \right] \quad (\text{C9})$$

where the variance $\sigma^2(M_h, z_h)$ smoothed at the scale $k(M_h)$ is defined as:

$$\sigma^2(M_h, z_h) = \int_0^\infty \frac{dk}{k} \frac{k^3 P_{\text{iso}}^{\text{PBH}}(z = z_h)}{2\pi^2} W^2(k, k(M_h)) \quad (\text{C10})$$

with $W(k, k(M_h))$ being the top-hat window function defined in Eq. (E1). This is valid when the Poissonian contribution to the power spectrum dominates over the adiabatic contribution. We find that for $m = 2.6 M_\odot$, $f_{\text{PBH}} = 1$, $k(M_h) = 400 \text{ Mpc}^{-1}$, $z_h = 30$, $F \sim 0.77$, meaning that already by the $z \sim 30$, more than half of the Poissonian fluctuations at this scale have collapsed to PBH clusters.

3. Dynamical heating of PBH clusters

Once a PBH cluster is formed, gravitational interactions between PBHs can lead to a gain in kinetic energy, via a process called dynamical heating, eventually causing the system to ‘‘puff up’’ or expand. This process is similar to the evolution properties of known gravitationally interacting systems, for example, star clusters. This effect was used in [53] (see also [141]) to constrain the abundance of massive compact halo objects (MACHOs) in ultra-faint dwarf galaxies. In our case, we consider the dynamical heating of PBH clusters, which causes the cluster radius to grow with time (see for example

Ref. [54]). Following [53, 54], in the case of a monochromatic PBH distribution, the time evolution of the cluster radius is governed by the following equation

$$\frac{dr_h}{dt} = \frac{4\sqrt{2} \pi G f_{\text{PBH}} m}{2v\beta r_h} \log \Lambda \quad (\text{C11})$$

$$\text{with } \log \Lambda \approx \log \left(\frac{r_h v^2}{G m} \right) \approx \log \left(\frac{M_h}{2 m} \right).$$

We assumed that the typical PBH velocity is of order of the virial velocity, $v \sim v_{\text{vir}}$ (see Eq. (B2)). In Eq. (C11), β is an $\mathcal{O}(1)$ factor that depends on the PBH cluster profile. We will set $\beta = 3.5$, which is the expected value for a PBH cluster following a NFW density profile, for consistency with the merger rate calculation. If one instead assumes a core profile, β changes by an order one factor, as well as the final cluster radius r_h . Uncertainties on the profile are taken into account in our free clustering parameter R_{cl} (see Sec. VB).

For a broad mass distribution, (obtained for example for spectral index $n_s = 0.965$), additional effects may come from the PBH mass segregation, with heavy PBHs sinking towards the center of the cluster and light PBHs moving towards the periphery. Numerical N-body simulations would be needed for fully detailed cluster dynamics and are out of the scope of the paper. We have followed Ref. [141] where the dynamical heating by PBHs of stars with a fixed mass in ultra-faint dwarf galaxies was considered for a broad PBH mass distribution and replaced the PBH mass dependent quantity, $f_{\text{PBH}} m \ln \Lambda$ in Eq. C11 by the averaged value over the mass function $\langle f_{\text{PBH}} m \ln \Lambda \rangle$, given by:

$$\langle f_{\text{PBH}} m \ln \Lambda \rangle = \int m f_{\text{PBH}}(m) \ln \Lambda d \ln m \quad (\text{C12})$$

with $f_{\text{PBH}}(m)$ defined in Eq. (7). Note that for our final solutions described in sec. V, we have approximated $\langle f_{\text{PBH}} m \ln \Lambda \rangle$ with $(f_{\text{PBH}} \langle m \rangle \ln \Lambda_{\text{avg}})$ with $\Lambda_{\text{avg}} = M_h/2\langle m \rangle$ and $\langle m \rangle$ being the average PBH mass weighted with the mass distribution (note that this is not the same as $\langle m \rangle$ defined in Eq. (16))

$$\langle m \rangle = \int m \phi(m) d \ln m. \quad (\text{C13})$$

Our results do not change with this approximation.

In Eq. (C11), we have neglected the competing cooling effect of any low mass particle like WIMP dark matter or even very light PBHs that could be present in the cluster. We consistently checked that this effect is indeed systematically smaller than the heating effect. Moreover, the total stellar mass in the typical PBH clusters is expected to be a negligible fraction of the total cluster mass [142]. For this reason we also neglect the heating effect induced by the stars.

In order to solve Eq. (C11), we set the initial radius size to the value at cluster formation (after the cluster

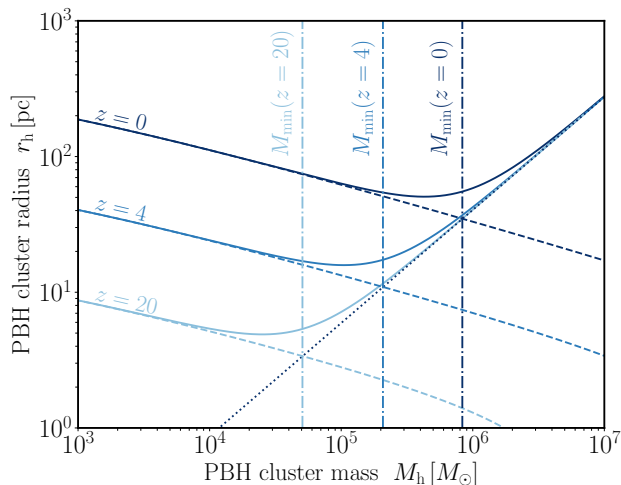


FIG. 7. Mass - radius relation given in Eq. (C14) (solid lines) of the PBH clusters at redshift values z fixed to 0, 4, 20. The large halo masses are unaffected by dynamical heating and follow the mass - radius relation at halo formation (dotted line) (given by Eq. (C8)). The lighter clusters progressively expand with time and are eventually diluted [54]. The dashed lines show the solution in Eq. (C14) with $r_h(t_c) = 0$. The minimum cluster mass $M_{\min}(z)$ (dotted dashed lines) is given by the intersection of the dotted and dashed lines at the corresponding redshift z . In this example, we have fixed $\langle f_{\text{PBH}} m \rangle = 3M_{\odot}$.

has virialized), given in Eq. (C8). Finally, we can write the PBH cluster radius at any time t as:

$$r_h(t)^{3/2} = r_h(t_c)^{3/2} + \frac{6\pi}{\beta} \sqrt{\frac{G}{M_h}} \langle f_{\text{PBH}} m \ln \Lambda \rangle (t - t_c) \quad (\text{C14})$$

where t_c denotes the time of collapse, at the redshift of cluster formation z_h . For large M_h , the first term in the RHS dominates, whereas for small M_h , the second term from heating will dominate.

In Fig. 7, we show the time evolution of the mass-radius relation for PBH clusters made of PBHs with fixed $\langle f_{\text{PBH}} m \rangle = 3M_{\odot}$. Initially the clusters follow the initial mass-radius relation given in Eq. (C8), with the halo radius growing with the halo mass. Progressively, the light clusters become affected by the dynamical heating and start expanding. As argued in Ref. [54], as the cluster expands, it gets disrupted and eventually diluted inside larger clusters. The heating effect is roughly suppressed as $\propto M_h^{-1/2}$ for heavier clusters. In Fig. 7, we show the minimum cluster mass $M_{\min}(z)$ as dashed vertical lines above which the expansion process is not relevant in increasing the cluster size. Numerically, we approximate the minima of Eq. (C14) or M_{\min} , by finding the halo mass for which the two terms in the R.H.S of Eq. (C14) are equal in magnitude. For those parameter values for

which the heating effect is very small i.e. the first term is much larger than the second, we set the minimum halo mass $M_{\min} \sim 10 \langle m \rangle$. Additionally, we impose for all scenarios that M_{\min} should always be larger than $\sim 10 \langle m \rangle$. As time passes, PBH clusters of heavier masses are heated, such that the minimal cluster mass depends on time: $M_{\min}(z)$.

4. Clustering factor $R_{\text{cl}}(z)$

In this section, we provide a calculation of the clustering factor that enters in Eq. 24. We can assemble Eqs. (19),(20),(22) to write:

$$R_{\text{cl}}(z) = \frac{4\pi^2}{3} \left(\frac{85\pi}{6\sqrt{2}} \right)^{2/7} \frac{G^2 \bar{\rho}_{\text{DM}}^2}{c^{10/7}} \int_{M_{\min}(z)}^{\infty} dM_h \quad (\text{C15}) \\ \times v_{\text{vir}}^{-11/7} \mathcal{F}_{\text{avg}} \mathcal{G}_{\text{NFW}} \tau_h^3 \delta_{\text{cl}}^2 \frac{dn(z)}{dM_h} \text{Gpc}^{-3} \text{yr}^{-1},$$

where \mathcal{G}_{NFW} is the factor associated to the radial integration of the NFW profile of the halo [102],

$$\mathcal{G}_{\text{NFW}} = \frac{C^3 (1 - 1/(1+C)^3)}{9 (\ln(1+C) - 1/(1+C))^2}, \quad (\text{C16})$$

while δ_{cl} parametrizes the overdensity of the halo compared to the background density,

$$\delta_{\text{cl}} = \frac{3M_h}{4\pi r_h^3 \bar{\rho}_{\text{DM}}}. \quad (\text{C17})$$

Note that here r_h corresponds to the cluster Virial radius at the time of cluster formation or collapse given by Eq. C15. Using the explicit expression of the halo mass function from Eq. (22), we can further simplify the clustering factor to

$$R_{\text{cl}}(z) = \sqrt{\pi} \left(\frac{85\pi}{6\sqrt{2}} \right)^{2/7} \frac{(G \Omega_{\text{DM}} \rho_c)^2}{c^{10/7}} \int_{M_{\min}(z)}^{\infty} dM_h \\ \times v_{\text{vir}}^{-11/7} \mathcal{F}_{\text{avg}} \mathcal{G}_{\text{NFW}} \delta_{\text{cl}} \sqrt{\frac{M_h}{M_*(z)} \frac{e^{-M_h/M_*}}{M_h}}. \quad (\text{C18})$$

This approach still contains a certain number of uncertainties and several physical effects may undermine the validity of this calculation, for instance the tidal disruption of clusters in the halo of massive galaxies, collisional disruptions, hierarchical mergers (see Ref. [54] for a discussion on this). This provides additional motivations to perform an analysis with a free value of R_{cl} .

Appendix D: Constraints on the Primordial Power Spectrum

1. μ -Distortions

In the analysis performed in Sec.V, we imposed the CMB μ -distortion constraints on the curvature power

spectrum at scales $k \lesssim 10^5 \text{ Mpc}^{-1}$ [56]. This is usually parameterized in terms of the parameter μ ,

$$\mu \approx \int_{1\text{Mpc}^{-1}}^{\infty} \frac{dk}{k} P_{\zeta}(k) W_{\mu}(k), \quad (\text{D1})$$

with the window function defined as

$$W_{\mu}(k) \approx 2.27 \left[\exp \left\{ \left(- \frac{(k/1360)^2}{(1 + (k/260)^{0.3} + k/340)} \right) \right\} - \exp \left\{ \left(- \left(\frac{k}{32} \right)^2 \right) \right\} \right], \quad (\text{D2})$$

where μ has been constrained by FIRAS/COBE [96, 97] to have the upper limit $\mu < 9 \times 10^{-5}$.

In our Bayesian inference, we systematically impose this μ -distortion constraint on the power spectrum in Eq. (3).

2. ΔN_{eff}

Since gravitational waves act as radiation, they are thus constrained by current bounds on the effective number of neutrino species limit, $\Delta N_{\text{eff}} < 0.28$ [143]. In our analysis, only the SIGWs will be subject to these constraints since the GWB from late PBH binaries will contribute after CMB. This will give the following constrain (see for e.g. [48]):

$$\int d \log(f) h^2 \Omega_{\text{gw}}^{\text{SIGW}}(f) < 5.6 \times 10^{-6} \Delta N_{\text{eff}}, \quad (\text{D3})$$

where $h^2 \Omega_{\text{gw}}^{\text{SIGW}}(f)$ is the scalar induced spectrum in the total spectrum defined in Eq. (30). The posteriors obtained in Sec. V satisfy this limit.

3. LVK-Constraint

Finally, the LVK constraint [144] (See also Refs. [145, 146]) imposes that, at $f_{\text{LVK}} = 25 \text{ Hz}$,

$$\Omega_{\text{gw}} \leq 1.7 \times 10^{-8}. \quad (\text{D4})$$

The posteriors obtained for the fixed clustering analysis in Fig. 8 do not violate this constraint. For $n_s > 1$, k_{max} cuts-off the scalar induced GWB at $f_{\text{max}} \sim 10^{-8} \text{ Hz}$, much below the LVK frequency range. While for the parameter space with $n_s \sim 1$, $\log_{10} A_{\zeta} \lesssim -1.9$ due to the $f_{\text{PBH}} \leq 1$ constraint which gives an Ω_{gw} satisfying the LVK bound. For the free clustering analysis posteriors for the case with both SIGWs and PBHs shown in Fig. 5, the same reasoning will apply for the parameter space corresponding to $n_s \geq 0.8$, where the signal is dominated

by the scalar induced GWs. Some parts of the parameter space where $n_s \leq 0.8$ corresponding to the GW spectrum originating from PBH binaries can violate the LVK bound. However, the GW background from PBH late binaries for the maximum posterior values satisfies the LVK bound given in Eq. (D4).

The best fit values used for the GW spectrum shown in Fig. 5 are in violation of this LVK bound.

Appendix E: Choice of Window Function

Here, we give the formulae for the window function $W(k', k)$ and the linear transfer function $T(k', k)$ used in Eq. (5) to define the variance σ_k^2 of overdensity δ . We want to reiterate here that the relic abundance of PBH exponentially depends on the variance, whose computation relies on the precise shape of the smoothing function W . For the choice of W , there is currently no prescription (see refs. [61, 65, 69, 147] for discussion on this). For our computation of the PBH abundance, we pick the Fourier transform of the real top-hat smoothing function which is one of the common choices used in literature. This window function can be written as:

$$W(k', k) = 3 \frac{\sin\left(\frac{k'}{k}\right) - \left(\frac{k'}{k}\right) \cos\left(\frac{k'}{k}\right)}{\left(\frac{k'}{k}\right)^3} \quad (\text{E1})$$

The linear transfer function instead used in Eq. 6 is given by [69]:

$$T(k', k) = 3 \frac{\sin\left(\frac{k'}{\sqrt{3}k}\right) - \left(\frac{k'}{\sqrt{3}k}\right) \cos\left(\frac{k'}{\sqrt{3}k}\right)}{\left(\frac{k'}{\sqrt{3}k}\right)^3} \quad (\text{E2})$$

Appendix F: Full Posterior Distributions

In this appendix, we describe the full parameter posterior distributions.

In the right panel of Fig. 8, we show the full 1d, 2d posterior distributions for the fixed clustering parameter analysis with $R_{\text{cl}} \equiv R_{\text{cl}}(A_{\zeta}, n_s, k_{\text{min}}, k_{\text{max}})$. As detailed in the main text, the clustering factor from Poissonian fluctuations is not large enough to enhance the the GW spectrum from PBH binaries. As a result, the 2d posterior region for which the PTA signal can have an important contribution from PBH binaries ($n_s \leq 0.8$) no longer exists. Only the 2d region with $n_s \geq 0.8$ remains, where the PTA GWB can be fitted with only scalar induced GWs (see Fig. 8 2d panel for $(\log_{10} A_{\zeta}, n_s)$).

In the left panel of Fig. 9, we show the complete 2d, 1d posterior distributions for free clustering factor analysis (see Section VB), including $(k_{\text{min}}, k_{\text{max}})$. As pointed out in the main text, two regions can be identified in the 2d posteriors for (A_{ζ}, n_s) for analysis including both SIGW and PBH binaries (blue): one for which the signal

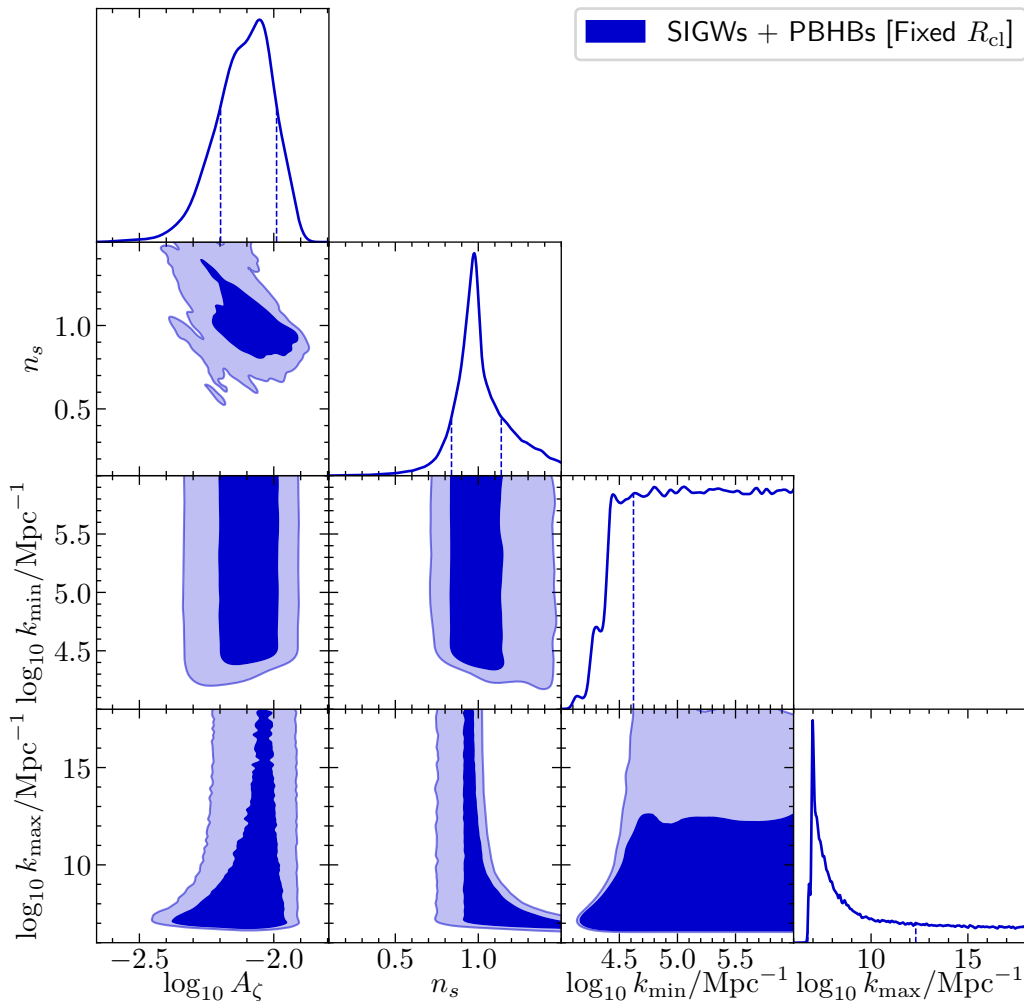


FIG. 8. Full posterior distributions for the fixed clustering factor analysis (see Section V A). The posteriors shown respect $f_{\text{PBH}} \leq 1$ as well as the CMB μ distortion limits from FIRAS/COBE [56].

λ	$\log_{10} A_\zeta$	n_s	$\log_{10} k_{\min}$	$\log_{10} k_{\max}$	$\log_{10} R_{\text{cl}}$
Prior	$[-4, -1]$	$[0.1, 1.5]$	$[4, 6]$	$[6, 18]$	$[0, 10]$

TABLE II. Model parameters and their prior range. The parameter R_{cl} is only employed for the free clustering factor analysis, see Section V B, and is otherwise computed using App. C 4.

is only fitted by SIGWs and a second for which SIGWs and PBH binaries coexist with similar amplitudes. Looking at the two-dimensional posteriors in (k_{\min}, n_s) , we indeed clearly see that for $n_s \geq 0.8$, the distribution becomes degenerated in k_{\min} . In this parameter space, the signal is fully captured by SIGWs and the GW spectrum is insensitive on k_{\min} . For $n_s \leq 0.8$ the GW spectrum from PBH binaries contribute to the signal and depends directly on the value of k_{\min} . The latter acting effectively as a large mass cutoff in the PBH mass function. The same conclusion applies for the posterior distribution in

(R_{cl}, n_s) .

In the same way, the parameter k_{\max} acts as a low mass cutoff. In the low spectral index region, $n_s \leq 0.8$ (where the signal is explained by both SIGWs and PBH binaries), the PBH mass function decays quickly at low masses and the parameter k_{\max} has little impact on it and therefore on the GW spectrum. For this reason, in this region the distribution is fully degenerated in k_{\max} (see (k_{\max}, n_s) panel). In the region where the signal is dominated by SIGWs ($n_s > 0.8$), and especially when $n_s > 1$, the light PBHs become a dominant part of the

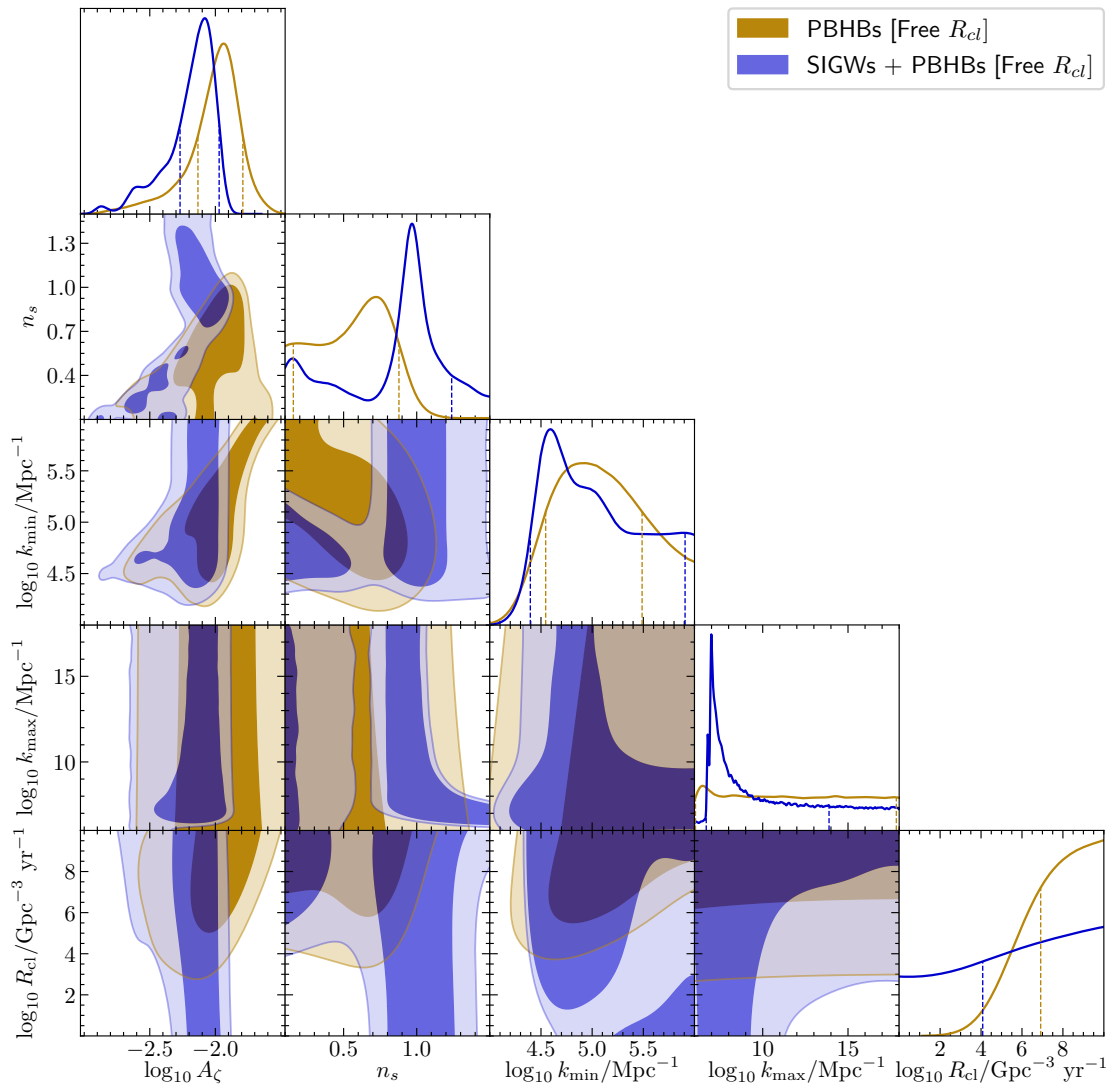


FIG. 9. Full posterior distributions for the free clustering factor analysis (see Section VB) for GWB from only PBH binaries (yellow) and GWB including SIGW (blue). The posteriors shown respect $f_{\text{PBH}} \leq 1$ as well as the CMB μ distortion limits from FIRAS/COBE [56].

PBH mass function. Even if the SIGW spectrum is insensitive on k_{max} , as n_s increases, the constraint $f_{\text{PBH}} \leq 1$

tends to impose a larger value for the cutoff k_{max} to prevent overclosure with light PBHs (see 2d posteriors for (k_{max}, n_s)).

-
- [1] Y. B. Zel'dovich and I. D. Novikov, The Hypothesis of Cores Retarded during Expansion and the Hot Cosmological Model, *Sov. Astron.* **10**, 602 (1967).
 - [2] S. W. Hawking, Black hole explosions?, *Nature* **248**, 30 (1974).
 - [3] G. F. Chapline, Cosmological effects of primordial black holes, *Nature* **253**, 251 (1975).
 - [4] B. J. Carr, The primordial black hole mass spectrum, *Astrophys. J.* **201**, 1 (1975).
 - [5] S. M. Leach, M. Sasaki, D. Wands, and A. R. Liddle, Enhancement of superhorizon scale inflationary curvature perturbations, *Phys. Rev. D* **64**, 023512 (2001), [arXiv:astro-ph/0101406](#).
 - [6] G. Ballesteros and M. Taoso, Primordial black hole dark matter from single field inflation, *Phys. Rev. D* **97**, 023501 (2018), [arXiv:1709.05565 \[hep-ph\]](#).
 - [7] S. S. Mishra and V. Sahni, Primordial Black Holes from a tiny bump/dip in the Inflaton potential, *JCAP* **04**,

- 007, [arXiv:1911.00057 \[gr-qc\]](#).
- [8] J. Liu, L. Bian, R.-G. Cai, Z.-K. Guo, and S.-J. Wang, Primordial black hole production during first-order phase transitions, *Phys. Rev. D* **105**, L021303 (2022), [arXiv:2106.05637 \[astro-ph.CO\]](#).
- [9] M. J. Baker, M. Breitbach, J. Kopp, and L. Mittnacht, Primordial Black Holes from First-Order Cosmological Phase Transitions, (2021), [arXiv:2105.07481 \[astro-ph.CO\]](#).
- [10] K. Kawana and K.-P. Xie, Primordial black holes from a cosmic phase transition: The collapse of Fermi-balls, *Phys. Lett. B* **824**, 136791 (2022), [arXiv:2106.00111 \[astro-ph.CO\]](#).
- [11] C. Gross, G. Landini, A. Strumia, and D. Teresi, Dark Matter as dark dwarfs and other macroscopic objects: multiverse relics?, *JHEP* **09**, 033, [arXiv:2105.02840 \[hep-ph\]](#).
- [12] J. Garriga, A. Vilenkin, and J. Zhang, Black holes and the multiverse, *JCAP* **02**, 064, [arXiv:1512.01819 \[hep-th\]](#).
- [13] B. Carr, K. Kohri, Y. Sendouda, and J. Yokoyama, Constraints on primordial black holes, *Rept. Prog. Phys.* **84**, 116902 (2021), [arXiv:2002.12778 \[astro-ph.CO\]](#).
- [14] S. Chandrasekhar, The Maximum Mass of Ideal White Dwarfs, *Astrophys. J.* **74**, 81 (1931).
- [15] M. Prunier, G. Mórás, J. F. N. n. Siles, S. Clesse, J. García-Bellido, and E. Ruiz Morales, Analysis of the subsolar-mass black hole candidate SSM200308 from the second part of the third observing run of Advanced LIGO-Virgo, (2023), [arXiv:2311.16085 \[gr-qc\]](#).
- [16] G. Mórás *et al.*, Analysis of a subsolar-mass compact binary candidate from the second observing run of Advanced LIGO, *Phys. Dark Univ.* **42**, 101285 (2023), [arXiv:2301.11619 \[gr-qc\]](#).
- [17] R. Abbott *et al.* (LIGO Scientific, VIRGO, KAGRA), Search for subsolar-mass black hole binaries in the second part of Advanced LIGO's and Advanced Virgo's third observing run, *Mon. Not. Roy. Astron. Soc.* **524**, 5984 (2023), [Erratum: *Mon. Not. Roy. Astron. Soc.* 526, 6234 (2023)], [arXiv:2212.01477 \[astro-ph.HE\]](#).
- [18] K. S. Phukon, G. Baltus, S. Caudill, S. Clesse, A. Depasse, M. Fays, H. Fong, S. J. Kapadia, R. Magee, and A. J. Tanasijczuk, The hunt for sub-solar primordial black holes in low mass ratio binaries is open, (2021), [arXiv:2105.11449 \[astro-ph.CO\]](#).
- [19] S. Clesse and J. Garcia-Bellido, GW190425, GW190521 and GW190814: Three candidate mergers of primordial black holes from the QCD epoch, *Phys. Dark Univ.* **38**, 101111 (2022), [arXiv:2007.06481 \[astro-ph.CO\]](#).
- [20] V. De Luca, V. Desjacques, G. Franciolini, P. Pani, and A. Riotto, GW190521 Mass Gap Event and the Primordial Black Hole Scenario, *Phys. Rev. Lett.* **126**, 051101 (2021), [arXiv:2009.01728 \[astro-ph.CO\]](#).
- [21] R. Abbott *et al.* (LIGO Scientific, Virgo), GW190814: Gravitational Waves from the Coalescence of a 23 Solar Mass Black Hole with a 2.6 Solar Mass Compact Object, *Astrophys. J. Lett.* **896**, L44 (2020), [arXiv:2006.12611 \[astro-ph.HE\]](#).
- [22] R. Abbott *et al.* (LIGO Scientific, Virgo), GW190521: A Binary Black Hole Merger with a Total Mass of $150M_{\odot}$, *Phys. Rev. Lett.* **125**, 101102 (2020), [arXiv:2009.01075 \[gr-qc\]](#).
- [23] E. Bagui *et al.* (LISA Cosmology Working Group), Primordial black holes and their gravitational-wave signatures, (2023), [arXiv:2310.19857 \[astro-ph.CO\]](#).
- [24] S. Pi and M. Sasaki, Gravitational Waves Induced by Scalar Perturbations with a Lognormal Peak, *JCAP* **09**, 037, [arXiv:2005.12306 \[gr-qc\]](#).
- [25] K. Inomata and T. Terada, Gauge Independence of Induced Gravitational Waves, *Phys. Rev. D* **101**, 023523 (2020), [arXiv:1912.00785 \[gr-qc\]](#).
- [26] K. Kohri and T. Terada, Semianalytic calculation of gravitational wave spectrum nonlinearly induced from primordial curvature perturbations, *Phys. Rev. D* **97**, 123532 (2018), [arXiv:1804.08577 \[gr-qc\]](#).
- [27] G. Agazie *et al.* (NANOGrav), The NANOGrav 15 yr Data Set: Observations and Timing of 68 Millisecond Pulsars, *Astrophys. J. Lett.* **951**, L9 (2023), [arXiv:2306.16217 \[astro-ph.HE\]](#).
- [28] G. Agazie *et al.* (NANOGrav), The NANOGrav 15 yr Data Set: Evidence for a Gravitational-wave Background, *Astrophys. J. Lett.* **951**, L8 (2023), [arXiv:2306.16213 \[astro-ph.HE\]](#).
- [29] J. Antoniadis *et al.* (EPTA, InPTA:), The second data release from the European Pulsar Timing Array - III. Search for gravitational wave signals, *Astron. Astrophys.* **678**, A50 (2023), [arXiv:2306.16214 \[astro-ph.HE\]](#).
- [30] J. Antoniadis *et al.* (EPTA), The second data release from the European Pulsar Timing Array - I. The dataset and timing analysis, *Astron. Astrophys.* **678**, A48 (2023), [arXiv:2306.16224 \[astro-ph.HE\]](#).
- [31] D. J. Reardon *et al.*, Search for an Isotropic Gravitational-wave Background with the Parkes Pulsar Timing Array, *Astrophys. J. Lett.* **951**, L6 (2023), [arXiv:2306.16215 \[astro-ph.HE\]](#).
- [32] H. Xu *et al.*, Searching for the Nano-Hertz Stochastic Gravitational Wave Background with the Chinese Pulsar Timing Array Data Release I, *Res. Astron. Astrophys.* **23**, 075024 (2023), [arXiv:2306.16216 \[astro-ph.HE\]](#).
- [33] J. Antoniadis *et al.*, The International Pulsar Timing Array second data release: Search for an isotropic gravitational wave background, *Mon. Not. Roy. Astron. Soc.* **510**, 4873 (2022), [arXiv:2201.03980 \[astro-ph.HE\]](#).
- [34] R. W. Hellings and G. S. Downs, Upper limits on the isotropic gravitational radiation background from pulsar timing analysis., *Astrophys. J. Lett.* **265**, L39 (1983).
- [35] A. Afzal *et al.* (NANOGrav), The NANOGrav 15 yr Data Set: Search for Signals from New Physics, *Astrophys. J. Lett.* **951**, L11 (2023), [arXiv:2306.16219 \[astro-ph.HE\]](#).
- [36] J. Ellis, M. Fairbairn, G. Franciolini, G. Hütsi, A. Iovino, M. Lewicki, M. Raidal, J. Urrutia, V. Vasconen, and H. Veermäe, What is the source of the PTA GW signal?, *Phys. Rev. D* **109**, 023522 (2024), [arXiv:2308.08546 \[astro-ph.CO\]](#).
- [37] V. De Luca, G. Franciolini, and A. Riotto, NANOGrav Data Hints at Primordial Black Holes as Dark Matter, *Phys. Rev. Lett.* **126**, 041303 (2021), [arXiv:2009.08268 \[astro-ph.CO\]](#).
- [38] K. Harigaya, K. Inomata, and T. Terada, Induced gravitational waves with kination era for recent pulsar timing array signals, *Phys. Rev. D* **108**, 123538 (2023), [arXiv:2309.00228 \[astro-ph.CO\]](#).
- [39] S. A. Hosseini Mansoori, F. Felegary, A. Talebian, and M. Sami, PBHs and GWs from T^2 -inflation and NANOGrav 15-year data, *JCAP* **08**, 067,

- arXiv:2307.06757 [astro-ph.CO].
- [40] Z. Yi, Z.-Q. You, Y. Wu, Z.-C. Chen, and L. Liu, Exploring the NANOGrav signal and planet-mass primordial black holes through Higgs inflation, *JCAP* **06**, 043, arXiv:2308.14688 [astro-ph.CO].
- [41] S. Balaji, G. Domènech, and G. Franciolini, Scalar-induced gravitational wave interpretation of PTA data: the role of scalar fluctuation propagation speed, *JCAP* **10**, 041, arXiv:2307.08552 [gr-qc].
- [42] D. G. Figueroa, M. Pieroni, A. Ricciardone, and P. Simakachorn, Cosmological Background Interpretation of Pulsar Timing Array Data, *Phys. Rev. Lett.* **132**, 171002 (2024), arXiv:2307.02399 [astro-ph.CO].
- [43] A. J. Iovino, G. Perna, A. Riotto, and H. Veermäe, Curbing PBHs with PTAs, *JCAP* **10**, 050, arXiv:2406.20089 [astro-ph.CO].
- [44] M. Braglia, J. Garcia-Bellido, and S. Kuroyanagi, Testing Primordial Black Holes with multi-band observations of the stochastic gravitational wave background, *JCAP* **12** (12), 012, arXiv:2110.07488 [astro-ph.CO].
- [45] G. Ferrante, G. Franciolini, A. Iovino, Junior., and A. Urbano, Primordial black holes in the curvaton model: possible connections to pulsar timing arrays and dark matter, *JCAP* **06**, 057, arXiv:2305.13382 [astro-ph.CO].
- [46] E. Madge, E. Morgante, C. Puchades-Ibáñez, N. Ramberg, W. Ratzinger, S. Schenk, and P. Schwaller, Primordial gravitational waves in the nano-Hertz regime and PTA data — towards solving the GW inverse problem, *JHEP* **10**, 171, arXiv:2306.14856 [hep-ph].
- [47] K. Inomata, K. Kohri, and T. Terada, Detected stochastic gravitational waves and subsolar-mass primordial black holes, *Phys. Rev. D* **109**, 063506 (2024), arXiv:2306.17834 [astro-ph.CO].
- [48] V. Dandoy, V. Domcke, and F. Rompineve, Search for scalar induced gravitational waves in the international pulsar timing array data release 2 and NANOGrav 12.5 years datasets, *SciPost Phys. Core* **6**, 060 (2023), arXiv:2302.07901 [astro-ph.CO].
- [49] P. F. Depta, K. Schmidt-Hoberg, P. Schwaller, and C. Tasillo, Do pulsar timing arrays observe merging primordial black holes?, (2023), arXiv:2306.17836 [astro-ph.CO].
- [50] Y. Gouttenoire, S. Trifinopoulos, G. Valogiannis, and M. Vanvlasselaer, Scrutinizing the primordial black hole interpretation of PTA gravitational waves and JWST early galaxies, *Phys. Rev. D* **109**, 123002 (2024), arXiv:2307.01457 [astro-ph.CO].
- [51] C. T. Byrnes, M. Hindmarsh, S. Young, and M. R. S. Hawkins, Primordial black holes with an accurate QCD equation of state, *JCAP* **08**, 041, arXiv:1801.06138 [astro-ph.CO].
- [52] A. Moradinezhad Dizgah, G. Franciolini, and A. Riotto, Primordial Black Holes from Broad Spectra: Abundance and Clustering, *JCAP* **11**, 001, arXiv:1906.08978 [astro-ph.CO].
- [53] T. D. Brandt, Constraints on MACHO Dark Matter from Compact Stellar Systems in Ultra-Faint Dwarf Galaxies, *Astrophys. J. Lett.* **824**, L31 (2016), arXiv:1605.03665 [astro-ph.GA].
- [54] B. Carr, S. Clesse, J. Garcia-Bellido, M. Hawkins, and F. Kuhnel, Observational evidence for primordial black holes: A positivist perspective, *Phys. Rept.* **1054**, 1 (2024), arXiv:2306.03903 [astro-ph.CO].
- [55] E. Bagui and S. Clesse, A boosted gravitational wave background for primordial black holes with broad mass distributions and thermal features, *Phys. Dark Univ.* **38**, 101115 (2022), arXiv:2110.07487 [astro-ph.CO].
- [56] J. Chluba, A. L. Erickcek, and I. Ben-Dayan, Probing the inflaton: Small-scale power spectrum constraints from measurements of the CMB energy spectrum, *Astrophys. J.* **758**, 76 (2012), arXiv:1203.2681 [astro-ph.CO].
- [57] B. B. P. Perera *et al.*, The International Pulsar Timing Array: Second data release, *Mon. Not. Roy. Astron. Soc.* **490**, 4666 (2019), arXiv:1909.04534 [astro-ph.HE].
- [58] T. Bringmann, P. F. Depta, V. Domcke, and K. Schmidt-Hoberg, Towards closing the window of primordial black holes as dark matter: The case of large clustering, *Phys. Rev. D* **99**, 063532 (2019).
- [59] M. Raidal, V. Vaskonen, and H. Veermäe, Gravitational Waves from Primordial Black Hole Mergers, *JCAP* **09**, 037, arXiv:1707.01480 [astro-ph.CO].
- [60] G. Ballesteros, P. D. Serpico, and M. Taoso, On the merger rate of primordial black holes: effects of nearest neighbours distribution and clustering, *JCAP* **10**, 043, arXiv:1807.02084 [astro-ph.CO].
- [61] S. Young, The primordial black hole formation criterion re-examined: Parametrisation, timing and the choice of window function, *Int. J. Mod. Phys. D* **29**, 2030002 (2019), arXiv:1905.01230 [astro-ph.CO].
- [62] B. Carr, S. Clesse, J. Garcia-Bellido, and F. Kuhnel, Cosmic conundra explained by thermal history and primordial black holes, *Phys. Dark Univ.* **31**, 100755 (2021), arXiv:1906.08217 [astro-ph.CO].
- [63] W. H. Press and P. Schechter, Formation of galaxies and clusters of galaxies by selfsimilar gravitational condensation, *Astrophys. J.* **187**, 425 (1974).
- [64] B. J. Carr, The Primordial black hole mass spectrum, *Astrophys. J.* **201**, 1 (1975).
- [65] A. D. Gow, C. T. Byrnes, P. S. Cole, and S. Young, The power spectrum on small scales: Robust constraints and comparing PBH methodologies, *JCAP* **02**, 002, arXiv:2008.03289 [astro-ph.CO].
- [66] M. W. Choptuik, Universality and scaling in gravitational collapse of a massless scalar field, *Phys. Rev. Lett.* **70**, 9 (1993).
- [67] J. C. Niemeyer and K. Jedamzik, Near-critical gravitational collapse and the initial mass function of primordial black holes, *Phys. Rev. Lett.* **80**, 5481 (1998), arXiv:astro-ph/9709072.
- [68] J. C. Niemeyer and K. Jedamzik, Dynamics of primordial black hole formation, *Phys. Rev. D* **59**, 124013 (1999), arXiv:astro-ph/9901292.
- [69] S. Young, I. Musco, and C. T. Byrnes, Primordial black hole formation and abundance: contribution from the non-linear relation between the density and curvature perturbation, *JCAP* **11**, 012, arXiv:1904.00984 [astro-ph.CO].
- [70] G. Franciolini, I. Musco, P. Pani, and A. Urbano, From inflation to black hole mergers and back again: Gravitational-wave data-driven constraints on inflationary scenarios with a first-principle model of primordial black holes across the QCD epoch, *Phys. Rev. D* **106**, 123526 (2022), arXiv:2209.05959 [astro-ph.CO].
- [71] A. Escrivà, C. Germani, and R. K. Sheth, Universal threshold for primordial black hole formation, *Phys. Rev. D* **101**, 044022 (2020), arXiv:1907.13311 [gr-qc].

- [72] I. Musco, Threshold for primordial black holes: Dependence on the shape of the cosmological perturbations, *Phys. Rev. D* **100**, 123524 (2019), [arXiv:1809.02127 \[gr-qc\]](#).
- [73] I. Musco, V. De Luca, G. Franciolini, and A. Riotto, Threshold for primordial black holes. II. A simple analytic prescription, *Phys. Rev. D* **103**, 063538 (2021), [arXiv:2011.03014 \[astro-ph.CO\]](#).
- [74] A. Escrivà, E. Bagui, and S. Clesse, Simulations of PBH formation at the QCD epoch and comparison with the GWTC-3 catalog, *JCAP* **05**, 004, [arXiv:2209.06196 \[astro-ph.CO\]](#).
- [75] V. Vaskonen and H. Veermäe, Did NANOGrav see a signal from primordial black hole formation?, *Phys. Rev. Lett.* **126**, 051303 (2021), [arXiv:2009.07832 \[astro-ph.CO\]](#).
- [76] G. Domènech, Scalar Induced Gravitational Waves Review, *Universe* **7**, 398 (2021), [arXiv:2109.01398 \[gr-qc\]](#).
- [77] K. N. Ananda, C. Clarkson, and D. Wands, The Cosmological gravitational wave background from primordial density perturbations, *Phys. Rev. D* **75**, 123518 (2007), [arXiv:gr-qc/0612013](#).
- [78] E. Bugaev and P. Klimai, Induced gravitational wave background and primordial black holes, *Physical Review D* **81**, 10.1103/physrevd.81.023517 (2010).
- [79] L. Alabidi, K. Kohri, M. Sasaki, and Y. Sendouda, Observable Spectra of Induced Gravitational Waves from Inflation, *JCAP* **09**, 017, [arXiv:1203.4663 \[astro-ph.CO\]](#).
- [80] D. Baumann, P. J. Steinhardt, K. Takahashi, and K. Ichiki, Gravitational Wave Spectrum Induced by Primordial Scalar Perturbations, *Phys. Rev. D* **76**, 084019 (2007), [arXiv:hep-th/0703290](#).
- [81] G. Domènech, S. Pi, A. Wang, and J. Wang, Induced Gravitational Wave interpretation of PTA data: a complete study for general equation of state, (2024), [arXiv:2402.18965 \[astro-ph.CO\]](#).
- [82] G. Franciolini, A. Iovino, Junior., V. Vaskonen, and H. Veermäe, Recent Gravitational Wave Observation by Pulsar Timing Arrays and Primordial Black Holes: The Importance of Non-Gaussianities, *Phys. Rev. Lett.* **131**, 201401 (2023), [arXiv:2306.17149 \[astro-ph.CO\]](#).
- [83] L. Liu, Z.-C. Chen, and Q.-G. Huang, Implications for the non-Gaussianity of curvature perturbation from pulsar timing arrays, *Phys. Rev. D* **109**, L061301 (2024), [arXiv:2307.01102 \[astro-ph.CO\]](#).
- [84] S. Wang, Z.-C. Zhao, J.-P. Li, and Q.-H. Zhu, Implications of pulsar timing array data for scalar-induced gravitational waves and primordial black holes: Primordial non-Gaussianity fNL considered, *Phys. Rev. Res.* **6**, L012060 (2024), [arXiv:2307.00572 \[astro-ph.CO\]](#).
- [85] C. Yuan, D.-S. Meng, and Q.-G. Huang, Full analysis of the scalar-induced gravitational waves for the curvature perturbation with local-type non-Gaussianities, *JCAP* **12**, 036, [arXiv:2308.07155 \[astro-ph.CO\]](#).
- [86] J. R. Espinosa, D. Racco, and A. Riotto, A Cosmological Signature of the SM Higgs Instability: Gravitational Waves, *JCAP* **09**, 012, [arXiv:1804.07732 \[hep-ph\]](#).
- [87] T. Nakamura, M. Sasaki, T. Tanaka, and K. S. Thorne, Gravitational waves from coalescing black hole MA-CHO binaries, *Astrophys. J. Lett.* **487**, L139 (1997), [arXiv:astro-ph/9708060](#).
- [88] K. Ioka, T. Chiba, T. Tanaka, and T. Nakamura, Black hole binary formation in the expanding universe: Three body problem approximation, *Phys. Rev. D* **58**, 063003 (1998), [arXiv:astro-ph/9807018](#).
- [89] M. Raidal, C. Spethmann, V. Vaskonen, and H. Veermäe, Formation and Evolution of Primordial Black Hole Binaries in the Early Universe, *JCAP* **02**, 018, [arXiv:1812.01930 \[astro-ph.CO\]](#).
- [90] V. Vaskonen and H. Veermäe, Lower bound on the primordial black hole merger rate, *Phys. Rev. D* **101**, 043015 (2020), [arXiv:1908.09752 \[astro-ph.CO\]](#).
- [91] G. Hütsi, M. Raidal, and H. Veermäe, Small-scale structure of primordial black hole dark matter and its implications for accretion, *Phys. Rev. D* **100**, 083016 (2019), [arXiv:1907.06533 \[astro-ph.CO\]](#).
- [92] P. Meszaros, Primeval black holes and galaxy formation, *Astron. Astrophys.* **38**, 5 (1975).
- [93] D. Inman and Y. Ali-Haïmoud, Early structure formation in primordial black hole cosmologies, *Phys. Rev. D* **100**, 083528 (2019), [arXiv:1907.08129 \[astro-ph.CO\]](#).
- [94] M. S. Delos, A. Rantala, S. Young, and F. Schmidt, Structure formation with primordial black holes: collisional dynamics, binaries, and gravitational waves, (2024), [arXiv:2410.01876 \[astro-ph.CO\]](#).
- [95] S. Clesse and J. García-Bellido, Seven Hints for Primordial Black Hole Dark Matter, *Phys. Dark Univ.* **22**, 137 (2018), [arXiv:1711.10458 \[astro-ph.CO\]](#).
- [96] J. C. Mather *et al.*, Measurement of the Cosmic Microwave Background spectrum by the COBE FIRAS instrument, *Astrophys. J.* **420**, 439 (1994).
- [97] D. J. Fixsen, E. S. Cheng, J. M. Gales, J. C. Mather, R. A. Shafer, and E. L. Wright, The Cosmic Microwave Background spectrum from the full COBE FIRAS data set, *Astrophys. J.* **473**, 576 (1996), [arXiv:astro-ph/9605054](#).
- [98] G. Hütsi, M. Raidal, V. Vaskonen, and H. Veermäe, Two populations of LIGO-Virgo black holes, *JCAP* **03**, 068, [arXiv:2012.02786 \[astro-ph.CO\]](#).
- [99] K. Kadota and J. Silk, Boosting small-scale structure via primordial black holes and implications for sub-GeV dark matter annihilation, *Phys. Rev. D* **103**, 043530 (2021), [arXiv:2012.03698 \[astro-ph.CO\]](#).
- [100] H. Mouri and Y. Taniguchi, Runaway merging of black holes: analytical constraint on the timescale, *Astrophys. J. Lett.* **566**, L17 (2002), [arXiv:astro-ph/0201102](#).
- [101] G. D. Quinlan and S. L. Shapiro, Dynamical Evolution of Dense Clusters of Compact Stars, *Astrophys. J.* **343**, 725 (1989).
- [102] S. Bird, I. Cholis, J. B. Muñoz, Y. Ali-Haïmoud, M. Kamionkowski, E. D. Kovetz, A. Raccanelli, and A. G. Riess, Did LIGO detect dark matter?, *Phys. Rev. Lett.* **116**, 201301 (2016), [arXiv:1603.00464 \[astro-ph.CO\]](#).
- [103] J. F. Navarro, C. S. Frenk, and S. D. M. White, The Structure of cold dark matter halos, *Astrophys. J.* **462**, 563 (1996), [arXiv:astro-ph/9508025](#).
- [104] A. D. Ludlow, S. Bose, R. E. Angulo, L. Wang, W. A. Hellwing, J. F. Navarro, S. Cole, and C. S. Frenk, The mass–concentration–redshift relation of cold and warm dark matter haloes, *Mon. Not. Roy. Astron. Soc.* **460**, 1214 (2016), [arXiv:1601.02624 \[astro-ph.CO\]](#).
- [105] F. Prada, A. A. Klypin, A. J. Cuesta, J. E. Betancort-Rijo, and J. Primack, Halo concentrations in the standard Λ CDM cosmology, *Mon. Not. Roy. Astron. Soc.* **423**, 3018 (2012), [arXiv:1104.5130 \[astro-ph.CO\]](#).
- [106] Y. Ali-Haïmoud, E. D. Kovetz, and M. Kamionkowski,

- Merger rate of primordial black-hole binaries, *Phys. Rev. D* **96**, 123523 (2017), [arXiv:1709.06576 \[astro-ph.CO\]](#).
- [107] V. De Luca, V. Desjacques, G. Franciolini, and A. Riotto, The clustering evolution of primordial black holes, *JCAP* **11**, 028, [arXiv:2009.04731 \[astro-ph.CO\]](#).
- [108] E. S. Phinney, A Practical theorem on gravitational wave backgrounds, (2001), [arXiv:astro-ph/0108028](#).
- [109] S. Clesse and J. García-Bellido, Detecting the gravitational wave background from primordial black hole dark matter, *Phys. Dark Univ.* **18**, 105 (2017), [arXiv:1610.08479 \[astro-ph.CO\]](#).
- [110] V. Mandic, S. Bird, and I. Cholis, Stochastic Gravitational-Wave Background due to Primordial Binary Black Hole Mergers, *Phys. Rev. Lett.* **117**, 201102 (2016), [arXiv:1608.06699 \[astro-ph.CO\]](#).
- [111] X.-J. Zhu, E. Howell, T. Regimbau, D. Blair, and Z.-H. Zhu, Stochastic Gravitational Wave Background from Coalescing Binary Black Holes, *Astrophys. J.* **739**, 86 (2011), [arXiv:1104.3565 \[gr-qc\]](#).
- [112] A. Mitridate, D. Wright, R. von Eckardstein, T. Schröder, J. Nay, K. Olum, K. Schmitz, and T. Trickle, PTArcade, (2023), [arXiv:2306.16377 \[hep-ph\]](#).
- [113] A. Mitridate, Ptarcade [10.5281/zenodo.7876430](#) (2023).
- [114] G. Desvignes *et al.* (EPTA), High-precision timing of 42 millisecond pulsars with the European Pulsar Timing Array, *Mon. Not. Roy. Astron. Soc.* **458**, 3341 (2016), [arXiv:1602.08511 \[astro-ph.HE\]](#).
- [115] Z. Arzoumanian *et al.* (NANOGrav), The nanograv nine-year data set: Observations, arrival time measurements, and analysis of 37 millisecond pulsars, *The Astrophysical Journal* **813**, 65 (2015).
- [116] R. N. Manchester *et al.* (PPTA), The parkes pulsar timing array project, *Publications of the Astronomical Society of Australia* **30**, [10.1017/pasa.2012.017](#) (2013).
- [117] D. J. Reardon *et al.*, Timing analysis for 20 millisecond pulsars in the Parkes Pulsar Timing Array, *Mon. Not. Roy. Astron. Soc.* **455**, 1751 (2016), [arXiv:1510.04434 \[astro-ph.HE\]](#).
- [118] R. A. Allsman *et al.* (Macho), MACHO project limits on black hole dark matter in the 1-30 solar mass range, *Astrophys. J. Lett.* **550**, L169 (2001), [arXiv:astro-ph/0011506](#).
- [119] M. Oguri, J. M. Diego, N. Kaiser, P. L. Kelly, and T. Broadhurst, Understanding caustic crossings in giant arcs: characteristic scales, event rates, and constraints on compact dark matter, *Phys. Rev. D* **97**, 023518 (2018), [arXiv:1710.00148 \[astro-ph.CO\]](#).
- [120] H. Kawai and M. Oguri, Constraints on primordial black holes from the observed number of Icarus-like ultrahigh magnification events, (2024), [arXiv:2411.13816 \[astro-ph.CO\]](#).
- [121] P. Mróz *et al.*, No massive black holes in the Milky Way halo, *Nature* **632**, 749 (2024), [arXiv:2403.02386 \[astro-ph.GA\]](#).
- [122] Y. Inoue and A. Kusenko, New X-ray bound on density of primordial black holes, *JCAP* **10**, 034, [arXiv:1705.00791 \[astro-ph.CO\]](#).
- [123] F. Ziparo, S. Gallerani, A. Ferrara, and F. Vito, Cosmic radiation backgrounds from primordial black holes, *Mon. Not. Roy. Astron. Soc.* **517**, 1086 (2022), [arXiv:2209.09907 \[astro-ph.CO\]](#).
- [124] M. Andrés-Carcasona, A. J. Iovino, V. Vaskonen, H. Veermäe, M. Martínez, O. Pujolàs, and L. M. Mir, Constraints on primordial black holes from LIGO-Virgo-KAGRA O3 events, *Phys. Rev. D* **110**, 023040 (2024), [arXiv:2405.05732 \[astro-ph.CO\]](#).
- [125] P. D. Serpico, V. Poulin, D. Inman, and K. Kohri, Cosmic microwave background bounds on primordial black holes including dark matter halo accretion, *Phys. Rev. Res.* **2**, 023204 (2020), [arXiv:2002.10771 \[astro-ph.CO\]](#).
- [126] D. Agius, R. Essig, D. Gaggero, F. Scarcella, G. Suzcowski, and M. Valli, Feedback in the dark: a critical examination of CMB bounds on primordial black holes, *JCAP* **07**, 003, [arXiv:2403.18895 \[hep-ph\]](#).
- [127] G. Facchinetti, M. Lucca, and S. Clesse, Relaxing CMB bounds on primordial black holes: The role of ionization fronts, *Phys. Rev. D* **107**, 043537 (2023), [arXiv:2212.07969 \[astro-ph.CO\]](#).
- [128] S. M. Koushiappas and A. Loeb, Dynamics of Dwarf Galaxies Disfavor Stellar-Mass Black Holes as Dark Matter, *Phys. Rev. Lett.* **119**, 041102 (2017), [arXiv:1704.01668 \[astro-ph.GA\]](#).
- [129] B. P. Abbott *et al.* (LIGO Scientific, VIRGO), GW170104: Observation of a 50-Solar-Mass Binary Black Hole Coalescence at Redshift 0.2, *Phys. Rev. Lett.* **118**, 221101 (2017), [Erratum: *Phys.Rev.Lett.* **121**, 129901 (2018)], [arXiv:1706.01812 \[gr-qc\]](#).
- [130] G. Franciolini, K. Kritos, E. Berti, and J. Silk, Primordial black hole mergers from three-body interactions, *Phys. Rev. D* **106**, 083529 (2022), [arXiv:2205.15340 \[astro-ph.CO\]](#).
- [131] I. Cholis, E. D. Kovetz, Y. Ali-Haïmoud, S. Bird, M. Kamionkowski, J. B. Muñoz, and A. Raccanelli, Orbital eccentricities in primordial black hole binaries, *Phys. Rev. D* **94**, 084013 (2016), [arXiv:1606.07437 \[astro-ph.HE\]](#).
- [132] M. Gorton and A. M. Green, Effect of clustering on primordial black hole microlensing constraints, *JCAP* **08** (08), 035, [arXiv:2203.04209 \[astro-ph.CO\]](#).
- [133] G. Franciolini, A. Kehagias, S. Matarrese, and A. Riotto, Primordial Black Holes from Inflation and non-Gaussianity, *JCAP* **03**, 016, [arXiv:1801.09415 \[astro-ph.CO\]](#).
- [134] C. Ünal, E. D. Kovetz, and S. P. Patil, Multimessenger probes of inflationary fluctuations and primordial black holes, *Phys. Rev. D* **103**, 063519 (2021), [arXiv:2008.11184 \[astro-ph.CO\]](#).
- [135] Y. Akrami *et al.* (Planck), Planck 2018 results. IX. Constraints on primordial non-Gaussianity, *Astron. Astrophys.* **641**, A9 (2020), [arXiv:1905.05697 \[astro-ph.CO\]](#).
- [136] D. Hooper, A. Ireland, G. Krnjaic, and A. Stebbins, Supermassive primordial black holes from inflation, *JCAP* **04**, 021, [arXiv:2308.00756 \[astro-ph.CO\]](#).
- [137] N. Afshordi, P. McDonald, and D. N. Spergel, Primordial black holes as dark matter: The Power spectrum and evaporation of early structures, *Astrophys. J. Lett.* **594**, L71 (2003), [arXiv:astro-ph/0302035](#).
- [138] R. Murgia, G. Scelfo, M. Viel, and A. Raccanelli, Lyman- α Forest Constraints on Primordial Black Holes as Dark Matter, *Phys. Rev. Lett.* **123**, 071102 (2019), [arXiv:1903.10509 \[astro-ph.CO\]](#).
- [139] J.-O. Gong and N. Kitajima, Small-scale structure and 21cm fluctuations by primordial black holes, *JCAP* **08**, 017, [arXiv:1704.04132 \[astro-ph.CO\]](#).
- [140] A. Kashlinsky, LIGO gravitational wave detection, pri-

- mordial black holes and the near-IR cosmic infrared background anisotropies, *Astrophys. J. Lett.* **823**, L25 (2016), [arXiv:1605.04023 \[astro-ph.CO\]](#).
- [141] A. M. Green, Microlensing and dynamical constraints on primordial black hole dark matter with an extended mass function, *Phys. Rev. D* **94**, 063530 (2016), [arXiv:1609.01143 \[astro-ph.CO\]](#).
- [142] J. D. Simon, The Faintest Dwarf Galaxies, *Ann. Rev. Astron. Astrophys.* **57**, 375 (2019), [arXiv:1901.05465 \[astro-ph.GA\]](#).
- [143] N. Aghanim *et al.* (Planck), Planck 2018 results. VI. Cosmological parameters, *Astron. Astrophys.* **641**, A6 (2020), [Erratum: *Astron. Astrophys.* 652, C4 (2021)], [arXiv:1807.06209 \[astro-ph.CO\]](#).
- [144] R. Abbott *et al.* (KAGRA, Virgo, LIGO Scientific), Upper limits on the isotropic gravitational-wave background from Advanced LIGO and Advanced Virgo's third observing run, *Phys. Rev. D* **104**, 022004 (2021), [arXiv:2101.12130 \[gr-qc\]](#).
- [145] S. Mukherjee and J. Silk, Can we distinguish astrophysical from primordial black holes via the stochastic gravitational wave background?, *Mon. Not. Roy. Astron. Soc.* **506**, 3977 (2021), [arXiv:2105.11139 \[gr-qc\]](#).
- [146] S. Mukherjee, M. S. P. Meinema, and J. Silk, Prospects of discovering subsolar primordial black holes using the stochastic gravitational wave background from third-generation detectors, *Mon. Not. Roy. Astron. Soc.* **510**, 6218 (2022), [arXiv:2107.02181 \[astro-ph.CO\]](#).
- [147] K. Ando, K. Inomata, and M. Kawasaki, Primordial black holes and uncertainties in the choice of the window function, *Phys. Rev. D* **97**, 103528 (2018), [arXiv:1802.06393 \[astro-ph.CO\]](#).